Ice-Templating: Integrative Ice Frozen Assembly to Tailor Pore Morphology of Energy Storage and Conversion Devices

Feng Zhao, Lin Lin, Jian Zhang, Jing Liu, Junyou Shi, Yann Le Godec, Alexandre Courac

Ice-Templating: Integrative Ice Frozen Assembly to Tailor Pore Morphology of Energy Storage and Conversion Devices

Feng Zhao, Lin Lin, Jian Zhang, Jing Liu, Junyou Shi, Yann Le Godec, Alexandre Courac

Abstract: Ice-templating, also known as directional freezing or freeze-casting, features the tunability of microstructure, the widely applicability of functional nanomaterials, and the fabrication of multiscale well-controlled biomimetic materials. Recently, integrating ice-templating with other materials' processing technologies (such as, spraying, spinning, filtration, and hydrothermal), it has been investigated to tailor pore morphology of scaffolds for emerging applications. Such integration endows materials with various structures (cellular, dendritic, and lamellar) and dimensions (0D, 1D, 2D, and 3D), which opens up a new avenue for improving material properties and developing new materials. Herein, this paper probes into the relationship of integrative ice frozen assembly with structure and describes the fundamental principles and synthesis strategies for preparing multi-scale materials with complex biomimetic structures via ice-templating. Focusing on ice crystal nucleation and growth, it summarizes the performance of ice-templating in constructing pore geometries. Additionally, the paper analyzes in depth the correlation between microstructure and macromorphology of final scaffolds, highlighting the application of integrative ice frozen assembly in electrochemical energy storage and conversion, and prospects for future research directions for this field.

Keywords: ice-templating, integrative ice frozen assembly, pore morphology, electrochemical energy storage and conversion

1. Introduction

The storage and conversion of renewable energy sources (such as, solar energy, wind energy, and tidal energy) are subjected to territoriality and intermittency and thus need to be improved for their highly-efficient utilization.[1,2] Developing new-generation devices is of prime significance to electrochemical energy storage and conversion, to which the construct of aligned channel structures with low tortuosity of such materials among all kinds of advanced renewable energy sources are vital, possessing the potential of addressing energy crisis and environmental problems.[3–5] Those with a disordered porous structure suffer from limited conductivity because the electrolyte ion/electron transport pathways are impeded, while those having a hierarchical lamellar structure are good choices for optimizing energy and power densities, cycling stability, and rate performance.[6,7] Further, the rational design of pore geometry is expected to prepare scaffolds with hierarchical structure owing to the fast ion/electron transporting pathways, the tunable surface active sites, and the large accessible areas. Considering the limitations of existing synthetic strategies, it is also required to make clear the correlation between microstructure and macromorphology, which is of great significance to improving material properties and developing new materials.

prepare promising electrochemical energy storage and conversion devices. This assembly method comprises the preparation of a homogeneous dispersion of solid particles, controlled curing, freeze-drying, and then densification through post-treatment, which ushers in scaffolds with an excellent hierarchical lamellar porous structure. It has attracted widespread attention for the tunability of microstructure, the widely applicability of functional nanomaterials, and the fabrication of multiscale well-controlled biomimetic materials.[8,9] The porous structures of final scaffolds fall into three categories, microporous (< 2 nm), mesoporous (2–50 nm), and macroporous (> 50 nm), according to the size of the ice crystals formed. Integrative ice frozen assembly is capable of enhancing the stability of the solid–liquid interface by regulating the temperature and concentration fields.[10] Besides, ice-templating makes the cooperative control of microstructure and macromorphology possible to reach a balance among precise structural control, scalability, and cost–effectiveness when integrated with other processing technologies.[11] Briefly, other materials' processing technologies followed by ice-templating to construct pore geometry can break through the traditional preparation processes, affording multi-scale scaffolds with desired macromorphology.

Herein, this review illustrates the advantages of integrative ice frozen assembly in achieving multi-scale pore geometry, briefly describes the fundamental principles of ice-templating in regulating porous structure, and introduces in detail the application of integrative ice frozen assembly (spray-freezing, freeze-spinning, ice-templating combined with filtration, integrating ice-templating with hydrothermal) to assemble various architectures. Moreover, it elaborates on the design of electrochemical energy storage and conversion devices (supercapacitor (SC), lithium-ion battery (LIB), solar-driven steam generator, and fuel cell) and discusses the future research directions of integrative ice frozen assembly. Considering the lack of understanding of quantitative matching between microstructure and macromorphology, this review focuses on the descriptions of pore geometry construction by integrative ice frozen assembly through the collation of existing data sources, unraveling the optimization function of the strategy in applications.

2. Fundamental principles of ice-templating

The fundamental principles of ice-templating (dynamics and thermodynamics) can guide the relationships between freezing direction and macromorphology. The freezing direction depends heavily on the nucleation and growth of ice crystals, which are two independent but sequential stages of ice formation.[12] Specifically, supercooled water nucleates and crystallizes in a cold finger, and then ice crystals grow continuously in different gradient directions through heat transfer, which facilitates the vertical and horizontal diffusion of dispersion and forms various pore morphologies (cellular, dendritic, and lamellar) (**Figure 1**a). Finally, the ice crystals sublimate at relatively low temperatures, and pressure is applied to frame porous scaffolds. The morphologies and characteristics of the porous scaffolds prepared by ice-templating are influenced by the solidification rate, which is controlled by the suspension,[13–15] cooling rate,[16] cooling direction,[8] temperature gradient,[9,17] and so on. To sum up, it is necessary to comprehensively understand the dynamics and thermodynamics of ice-templating for further investigating the assembly process in Figure 1b.

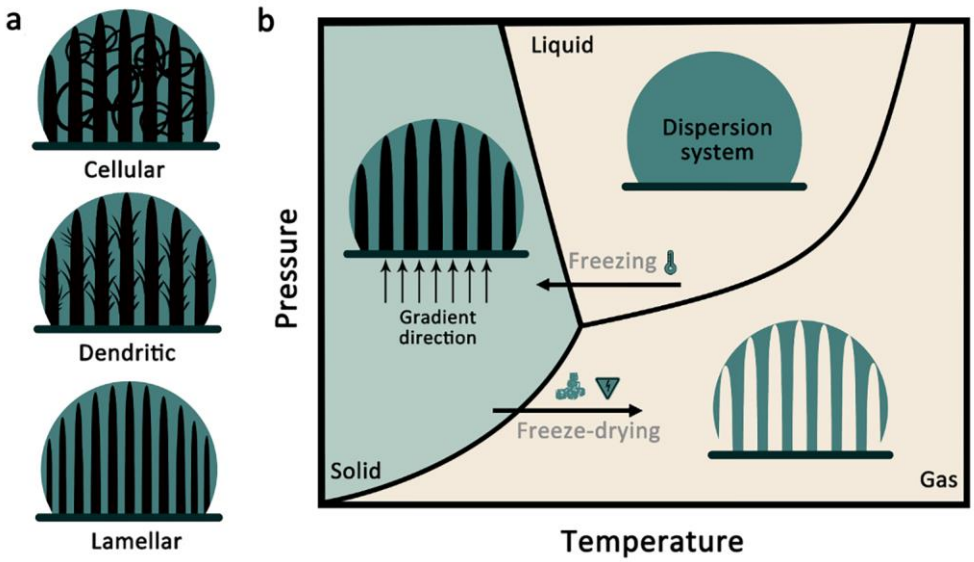

Figure 1. a) Different ice crystal morphologies in ice-templating. b) Schematic diagram of the fundamental principles of ice-templating. Black represents ice crystals, teal represents dispersion system.

2.1. Stability of solid–liquid interface

Ice-templating is a simple, adaptable, and effective processing technology that can design various pore geometries by fine-tuning the physical interactions between ice crystals and dispersion.[18] Surface force dominates the interactions between scattered particles in the dispersion, combined with fluid mechanics causing the particles to attract each other and aggregate into clusters, or repel each other and stably disperse, which facilitates the formation of ice nucleus (**Figure 2**a).[19] Ice crystallization is mainly governed by heterogeneous nucleation under the Brownian limit, and the flatness of the ice crystal shape at the solid–liquid interface is unstable (Figure 2b).[20]

As ice nucleus begin to form in unidirectional freezing, during which the displacement of particles and ice crystals occurs at the solid–liquid interface (Figure 2c), the solidification temperature changes, and this region is ultimately driven into a constitutionally supercooled metastable state.[21] When the particle displacement rate is greater than the ice crystal growth rate, the ice crystals gradually move from the solid phase to the liquid phase in the cold finger to increase the contact area, and the solid particles are repelled by the ice crystals and separated from the moving solidification front (Figure 2d). At the same time, the moving interface will inevitably encounter disturbance in the growth of ice crystals. In light of the Muffins-Sekerka interface stability theory, it can be understood how the disturbance behaves over time in the temperature and concentration fields, which interrupts the planar front and turns it into a stable nonplanar ice front.[22] These columnar ice crystals will branch to form dendrites, eventually reaching a steady state (Figure 2e). Therefore, the interactions of the solid-liquid interface are introduced into the system, and further considering how the ultimate pore geometries of scaffolds control depend on how the generation of ice crystals.

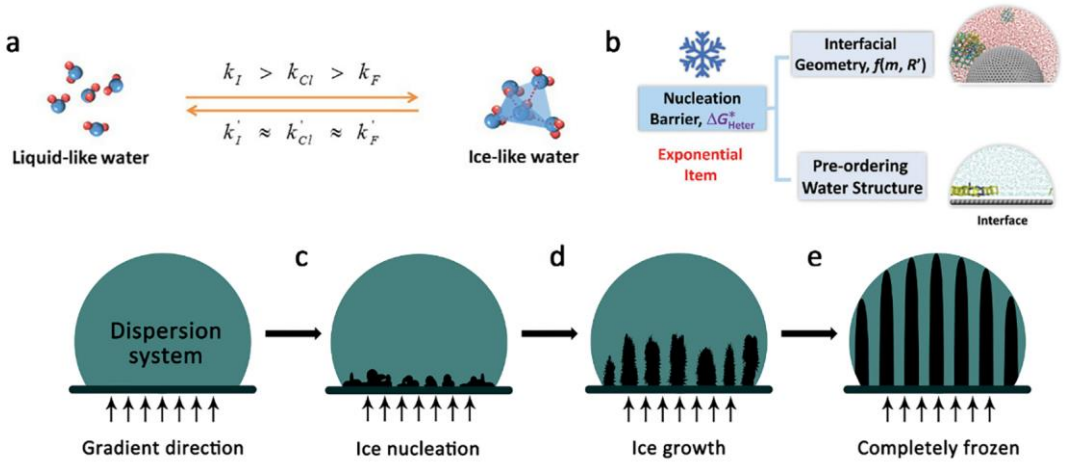

Figure 2. a) Water molecules at the solid–liquid interface undergoing structural change. Reproduced with permission.[23] Copyright 2018, American Chemical Society. b) Control of the heterogeneous ice nucleation barrier. Reproduced with permission.[24] Copyright 2018, The Royal Society of Chemistry. c–e) Schematic diagram of ice crystal growth in unidirectional freezing. Black represents ice crystals, teal represents dispersion system.

2.2. Dynamics of ice crystal growth

The self-assembly process accompanied by the microscopic morphological evolution of the solid–liquid interface is a typical kinetic problem (i.e., the physical interaction between the ice fronts and the solid particles) during the solidification of the dispersion.[25] Ice formation typically starts with heterogeneous nucleation on solid surfaces, and the key variable that determines whether there is displacement or entrapment between ice crystals and solid particles is the critical freezing front velocity (v_{cr}, Equation (1)), which helps analyze the force balance of both repulsive and attractive forces.[26–30] Understanding how the solid–liquid interface influences subsequent ice growth is critical.[25]

$$v_{cr} = \frac{\Delta\sigma_0 d}{3\eta r}\left(\frac{\alpha_0}{d}\right)^n \quad (1)$$

where r is the radius of solid particle, η is the dynamic viscosity of the dispersion, $\Delta\sigma_0$ is the interfacial free energy, α_0 is the average intermolecular distance in the liquid phase, d is the vertical distance between solid particles and the solidification front, and n is an empirical correction factor of the repulsive forces between 1 and 4.[29,31]

The freezing front velocity is denoted as v herein (**Figure 3**a). If $v \ll v_{cr}$, the growing ice crystals would displace the solid particles and make them separate from the solidification front, which increases the particle concentration in the unfrozen region. When $v < v_{cr}$, the ice-growth proceeds will be resisted by the solid particles, and repelling between them, resulting in lamellar walls within the scaffold. If $v \geq v_{cr}$, the majority of the particles will produce lamellar walls, while part of the particles will be entrapped in ice crystals as bridges between the lamellar walls, with fine-scale porosity formed. In the case of $v \gg v_{cr}$, the rapid-forming ice crystals fail to interact with the solid particles from the dispersion, leading to complete encapsulation of the particles with the ice front.[31,32] Occasionally, controlling ice nucleation and growth is crucial in the assembly process, in which the ordered porosity of anisotropic structure is constructed by simply replicating the ice crystal morphology. Therefore, different synthesis and processing technologies exert various v_{cr} during freezing and eventually assume distinct porous characteristics in integrated ice frozen assembly.

Ice growth is a tenacious mechanism and ice will continue to grow, as long as the temperature allows, until the resistance forces exceed the pushing force applied by the growing crystals. In displacement dominant systems, ice growth would stop when the concentrated particles on the surface of the ice crystals are wedged between multiple ice crystals. The critical freezing front velocity depends on the temperature gradient, freezing rate, solvent

composition, solute viscosity, and particle size. The interconnectedness between different variables creates various feasible conditions for solid particles to control ice crystal growth, as long as the temperature allows, as the number of particles or particle size increases, which is conducive to yielding smaller pores with thicker lamellae (Figure 3b).[33] Specifically, ice-templating is used to the ice crystals nucleating on a cold surface and preferential growing along the temperature gradient direction, which strikes a balance between precise structural control, effective scalability, and low cost. Thus, in the assembly process, the dynamics of ice crystal growth plays a vital role in determining the solid particles displacement or entrapment to achieve excellent microstructural characteristics and pore morphology.

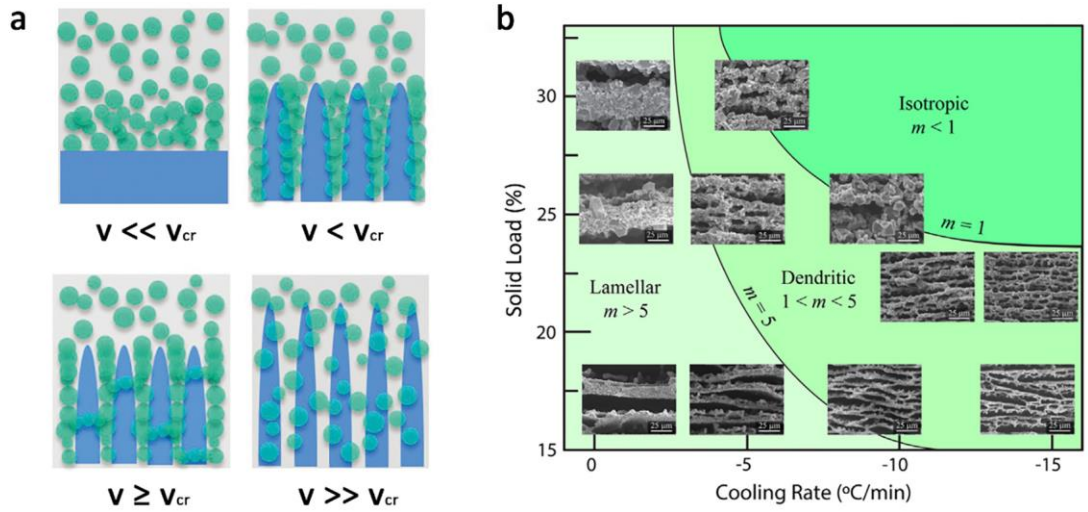

Figure 3. a) Growth of the solidification front at different interface velocities. Reproduced with permission.[9] Copyright 2020, Wiley-VCH. b) Combined effect of solidification rate and solute concentration on pore morphology. Reproduced with permission.[33] Copyright 2013, Elsevier.

2.3. Thermodynamics of ice formation

Ice formation contains two independent but sequential stages (ice crystal nucleation and growth).[8] The latent heat of phase transition is generated, and the volume expands (i.e., first-order phase transition) during the transformation of liquid water into solid ice, which is a transition from quantitative change to qualitative change. This nature transition can be controlled by varying the temperature gradient and cooling rate, which in turn influences the solidification rate. Thus, understanding how to precisely control the pore morphology, as well as the spacing and thickness of the scaffold walls, is critical.[34,35] As the temperature decreases to a certain level, the thermal motion of solid particles no longer destroys the thermodynamic interaction, at which point the thermodynamic characteristics of pore morphology can be determined according to Fourier's law (the law of thermal conduction, Equation (2)):

$$q = -k\frac{dT}{dx} \tag{2}$$

where is the heat flux (i.e., the rate of heat transfer per unit area on the *x*-axis perpendicular to the thermal transport direction direction), T is the temperature; x is the coordinate in the heat transfer direction, and k is the thermal conductivity coefficient. The temperature gradient (dT/dx) is proportional to q in Equation (2), but the direction of heat flow is opposite to that of the temperature gradient.[36–37] Similar to how a dynamic behavior of diffusion drives solid particle displacement and entrapment, thermal conduction controls heat exchange rate that affects solidification velocity, which in turn depends on the cooling rate and dispersion system.

Furthermore, the thermal equilibrium between solid particles in the dispersion results in Equation (3):

$$q = \rho\frac{dx}{dt}h \tag{3}$$

where ρ is the density of ice, h is the removal of latent heat, and t is time.[37] Alteration of thermal followability with

the change of the size and concentration of solid particles, thereby affecting ice particles approaching the thermal equilibrium states and, ultimately, ice crystal size.

Typically, ice formation can be divided into four thermal events, namely supercooling (i.e., a non-equilibrium, metastable state below the freezing point (T_f), beneficial for rapid formation of ice crystals, **Figure 4**a_0,a_1), ice crystal nucleation (the removal of latent heat, Figure 4a_1,a_2), ice crystal growth (a thermal plateau, Figure 4a_2,a_3), and complete crystallization or solidification (the removal of sensible heat, Figure 4a_3,a_4). On the other hand, aqueous solutions have similar performance in ice formation, which can promote heterogeneous nucleation and lower the initial freezing point (according to Raoul's law) to suppress all other thermal processes in the solutions, as illustrated in Figure 4a_0–a'_4.[10,38] Moreover, with the freezing temperature changing, ice crystals exhibit different crystallization forms (19 kinds), whereas the hexagonal form (I_h) is predominant in nature (Figure 4b). The first-order phase transition occurs when liquid water turns into solid ice, during which ice crystals begin to appear at the condensation point, and the solid–liquid interface is at equilibrium.[39,40] However, although the ice phase remains relatively stable in this situation, it is not in the thermodynamically most stable state according to the stability limit conjecture (regarding the phase boundary of the metastable phase).[41]

So far, applying a directed thermal gradient has been able to create a temporary lamellar template by inducing in situ ice crystal nucleation and growth inside the dispersion. Under the imposed thermal gradient in freezing technology, ice has growth potential in different directions. As a result, the change in material state (the latent heat of phase transition) alters the critical freezing front velocity, which ultimately influences the microstructure and macromorphology of the scaffolds.

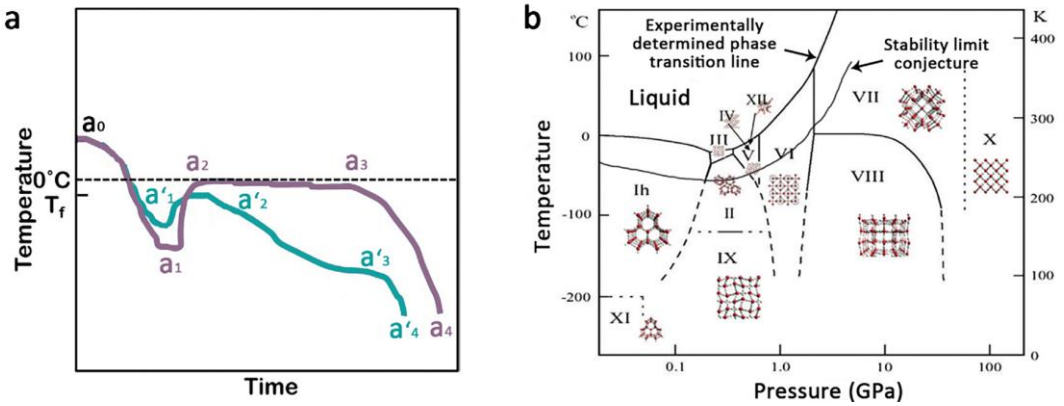

Figure 4. a) Thermal events of ice formation. Reproduced with permission.[38] Copyright 2002, Elsevier. b) Phase diagram of ice/water. Reproduced with permission.[24] Copyright 2018, The Royal Society of Chemistry. Reproduced with permission.[42] Copyright 2012, American Physical Society. Reproduced with permission.[43] Copyright 2002, Springer Nature.

2.4. Nature and concentration of suspension

The nature of suspension, one of the essential parameters to control pore morphology via ice templating, obtains a variety of porous structures by proper selection of solvents. For instance, Deville has investigated that the functional properties of pore morphology are diverse depending on the nature of suspensions from ceramics, polymers, metals, and composites because of the material-agnostic nature of the freezing route.[44] The mechanisms behind dynamics of ice crystal growth and thermodynamics of ice formation effects on pore morphology have yet to be investigated. Besides, its content can also play a huge role in controlling the porous structure and porosity compared to the nature of suspension. For suspensions with the same solid loading, tuning the concentrations of colloid solutions by varying the effect of change in the concentration of suspension to ice assembly process is beneficial for designing colloidally stable structures. For example, Bhattacharya et al. have reported the effect of concentration for constructing the

crosslinked oxygen functional groups of ozonated multiwall carbon nanotube (MWCNT).[45] The sheet dimension and structural regularity increase according to the spider-web-like MWCNT networks prepared from low to high sediment concentrations of MWCNT dispersion. The experimental results reveal that the connected porosity of the biomimetic composites is proportional to the initial concentration. Moreover, spider-web-like structure is collapsed due to the physical crosslinking of the oxygen functional groups is much lower at below a critical concentration. Similarly, functional nanomaterials with different particle sizes in suspension have different solidification temperatures and crystal morphologies, and the thermal stability of particles has a critical impact on the final pore morphology of the material. The surface energy of the larger particle size needs more energy from outside to escape the energy traps, implying that particles with a larger size have obtained the larger pore dimensionality of porous materials during freezing. Therefore, larger particles deposition at the bottom of the suspensions in a pressure-driven flow before freezing further affects the interaction between particles and ice crystals at the solidification front and is not conducive to fabricating hierarchical lamellar porous structures.

2.5. Freezing temperature

Independently from other factors (dispersion system, freezing direction, and thermal conductivity), the freezing temperature for ice formation should be adjusted to regulate the porous structures of the scaffolds, whose microstructure can be thereby made uniform.[11,46,47] Noteworthily, an excessively high freezing temperature will decrease the moving rate of the front of the solid–liquid interface and promote ice crystal growth to form a 3D scaffold structure with large-sized pores, while an overly low freezing temperature will induce ice crystal nucleation, thus influencing the solidification rate of ice crystals and causing changes in their structure (small-sized pores and thin walls).[13,28,48] Just so, this compact structure might have better mechanical properties to prevent collapse.

As shown in **Figure 5**a, Gao et al. directly assembled monodispersed silver nanowires (AgNWs) into interconnected 3D compartmentalized microstructures by unidirectional freezing.[49] Moreover, the pore orientation can be designed by utilizing suitable molds of different shapes. Thus, fine-tuning the microstructure and macromorphology of scaffolds is feasible, which is beneficial for improving mechanical properties.[50] The scanning electron microscope (SEM) images (Figure 5b–d) show that the pore size decreased, while the number of pores increased, with the pore wall becoming thinner, as the freezing temperature declined, indicating that frozen structures were temperature-dependent. The research provides theoretical guidance for designing stretchable and foldable conductors with high electromechanical stability. The mechanical properties of scaffolds with a multi-dimensional architecture might be improved by optimizing the linking of microstructure associated with freezing temperature, which are all important for the practical application of high-performance, hierarchical lamellar composites.

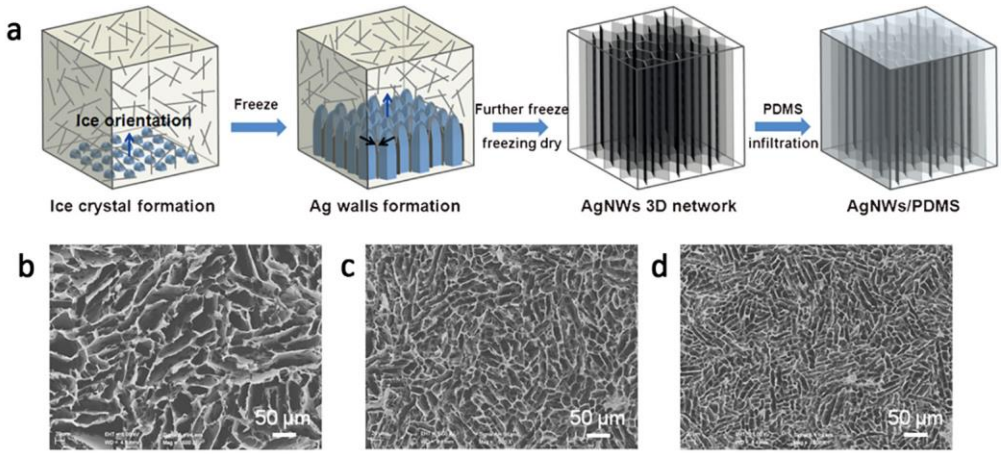

Figure 5. a) Schematic illustration of the formation mechanism of the 3D AgNW compartmentalized architecture by ice-templating,

b–d) SEM images of microstructures prepared at b) −10 °C, c) −30 °C, d) −50 °C. Reproduced with permission.[49] Copyright 2014, Wiley-VCH.

2.6. Freezing direction

Ice-templating is a simple and effective technique for producing multi-scale orderly porous structures by controlling ice crystal nucleation and growth, although the ice formation mechanism is stochastic. The solidification rate plays a key role in ice formation, which influences the ice crystal size and, ultimately, the pore size of the scaffold. There are four types of ice crystal nucleation and growth (i.e., freezing direction). As displayed in **Figure 6**, uniform cooling (nondirectional freezing) typically results in a stochastic isotropic porous structure, cooling a single surface (unidirectional freezing) yields a honeycomb-like structure with homogeneous alignment, bidirectional freezing constructs a long-range aligned lamellar structure, radial freezing of the extroverted type and introverted type forms uniformly graded aligned structure.[51–56]

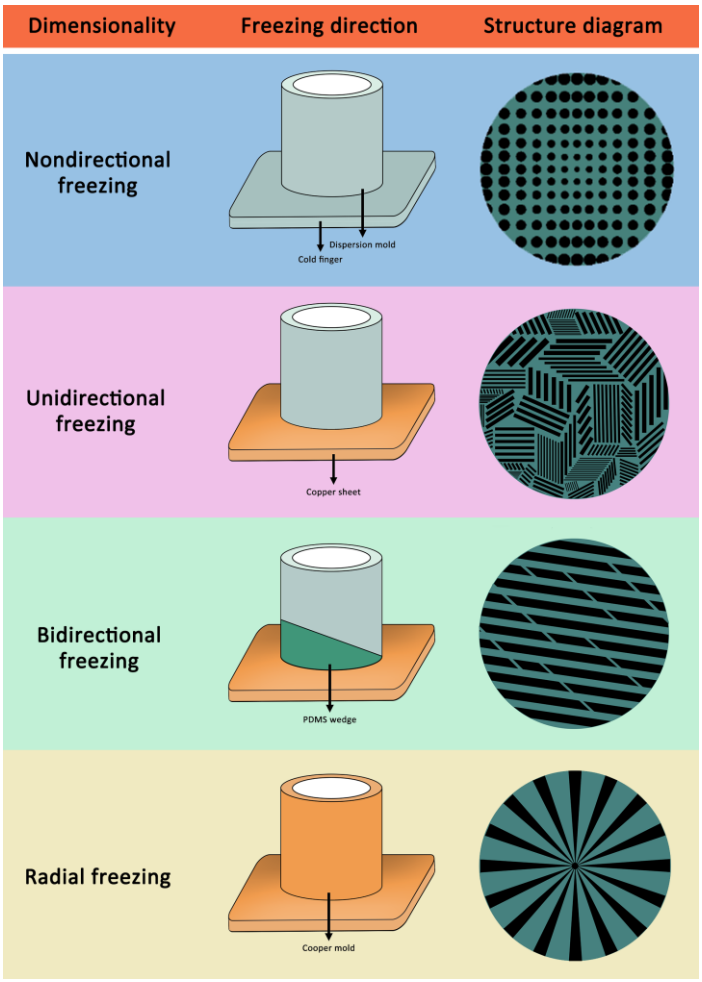

Figure 6. Relationship between structural diversification and freezing direction of ice-templating. Black represents ice crystals, teal represents dispersion system.

2.6.1. Nondirectional freezing

Concerning the simple nondirectional freezing, the mechanical interaction between the particles at the solid–liquid interface leads to randomly distributed ice crystals, thus forming isotropic structures. Usually, the dispersion is immediately placed in a thermostated environment (refrigerator, low-temperature thermostatic bath, and liquid

nitrogen freezing) to develop an isotropic composite material. Despite the fact that the environment is kept at a low temperature which meets the requirements for rapid freezing, the stochastic isotropic porous structure is the result of joint actions of the dispersion system, freezing rate, temperature gradient, and other factors. In other words, the factors influencing the structure are numerous, which is detrimental to a deep understanding of the preparation of hierarchical porous structures.[57] A dense network structure can be formed after the sublimation of small ice crystals, packing of particles, and doping of other cohesive materials. At the same time, the compact structure may collapse and make the mass transfer conditions deteriorate owing to the effect of mechanical properties. Accordingly, to further improve the usage effectiveness and structural properties of functional nanomaterials, researchers have fabricated various multi-scale 3D structures by ice-templating undergoing regulation at varying levels.

2.6.2. Unidirectional freezing

Compared with randomly oriented porous structures, scaffolds formed by unidirectional freezing with vertically arranged porous microarchitecture have improved physicochemical and mechanical properties, which is a typical apparatus that compels the ice crystals to contact with each other preferentially from the bottom to the top by cooling a single surface of the slurry.[57,58] With the advancement of freezing technology and novel materials, numerous innovative applications and improvements have been achieved by unidirectional freezing. As shown in **Figure 7**a, Xie et al. immersed the cold finger (copper rods of a cylindrical shape) in the cold source and made it cooperate with the heating resistor to produce a temperature gradient normal to the copper rods. Simultaneously, the mold was wrapped in a sponge with outstanding thermal insulation performance at its surrounding and bottom, and then the materials were placed in the cold finger, with the operating temperature of the cryogenic freezer adjusted by the thermocouple controllers (Figure 7b).[12] Zhao et al. poured the dispersion into the designed mold and observed the unidirectional freezing of ice crystals from the bottom to the top of the mold (Figure 7c).[59] The interaction of ice crystals at the solidification front transformed acrylamide (AAm) monomers into polyacrylamide (PAAm) hydrogels with a well-oriented structure via in situ cryopolymerization, and subsequently freeze-drying, the hydrogel was transformed into the aerogel to afford an excellent 3D honeycomb-like structure. What's notable is the development of pore morphology from lamellar to dendritic to cellular as the cooling rate increases. This can be explained by the fact that solidification velocity and resistance to growth is the key factor determining the nucleation and growth of ice crystals. However, the unidirectional freezing technology is defective in controlling the spatial behavior of single particles, and the combined use with freezing strategies in other directions is needed to make up for the shortage.

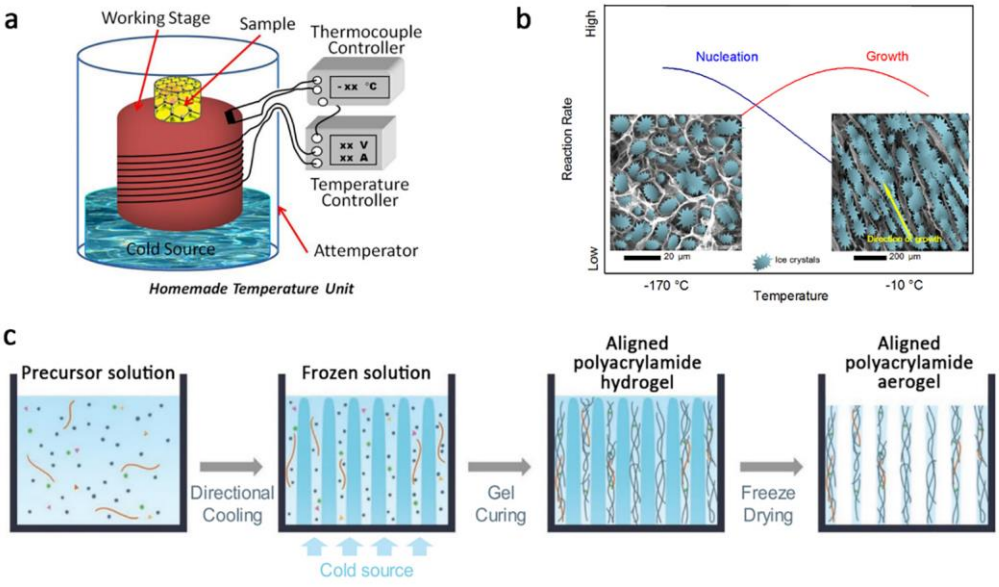

Figure 7. a) Schematic of the unidirectional freezing temperature unit and b) qualitative schematic of the ice crystal nucleation and growth as a function of freezing temperature. Reproduced with permission.[12] Copyright 2013, Springer Nature. c) Schematic of the fabrication of all-solid-state aerogel. Reproduced with permission.[59] Copyright 2020, Wiley-VCH.

2.6.3. Bidirectional freezing

In recent years, some researchers have designed and developed complex frameworks with lamellar structures by bidirectional freezing (potential bionic manufacturing technology), which have mechanical properties similar to those of numerous natural porous materials from microstructure to macromorphology.[60] Bai et al. appropriately regulated the nucleation and growth of ice crystals under the dual temperature gradients and created polydimethylsiloxane (PDMS) wedges with different slopes to cover the cold finger (**Figure 8**a,b).[61] Completely separating ice crystals and nanoparticles by utilizing the PDMS wedge achieved a centimeter-scale nacre-mimetic composite, in which ice crystals nucleation was only at the line near the bottom of the PDMS wedge modifying the cold finger, i.e., one-dimensional nucleation (Figure 8c). The temperature gradient during freezing can be decomposed into vertical and horizontal components, which revealed the temperature difference between the bottom and the top of the PDMS wedge (colder at the bottom than at the top) (Figure 8d). Unlike the other cooling element systems, the bidirectional freezing on the cold finger surface results in improved uniformity in the architecture of the resulting porous material.

Meanwhile, we further highlight the freezing temperature and freezing rate of the slurry moving on the surface of the cooling element under various wettability gradients can overcome the size limitation resulting from the PDMS wedge. For example, Zhao et al. obtained a cross-aligned lamellar structure by introducing a wettability gradient to control ice nucleation and growth on cold surfaces (Figure 8e,f).[8] In addition, a linear wettability gradient occurs with the water contact angle along a perpendicular direction. This suggests that the orientations of ice crystals are determined by the wettability gradient surfaces rather than the type of surface material. Accordingly, hierarchical lamellar porous composites, which combine multiple pore systems from nano-, micro- to macro-regimes, have opened up new possibilities for the digital design and manufacturing of lamellar porous structures for various applications.[62,63]

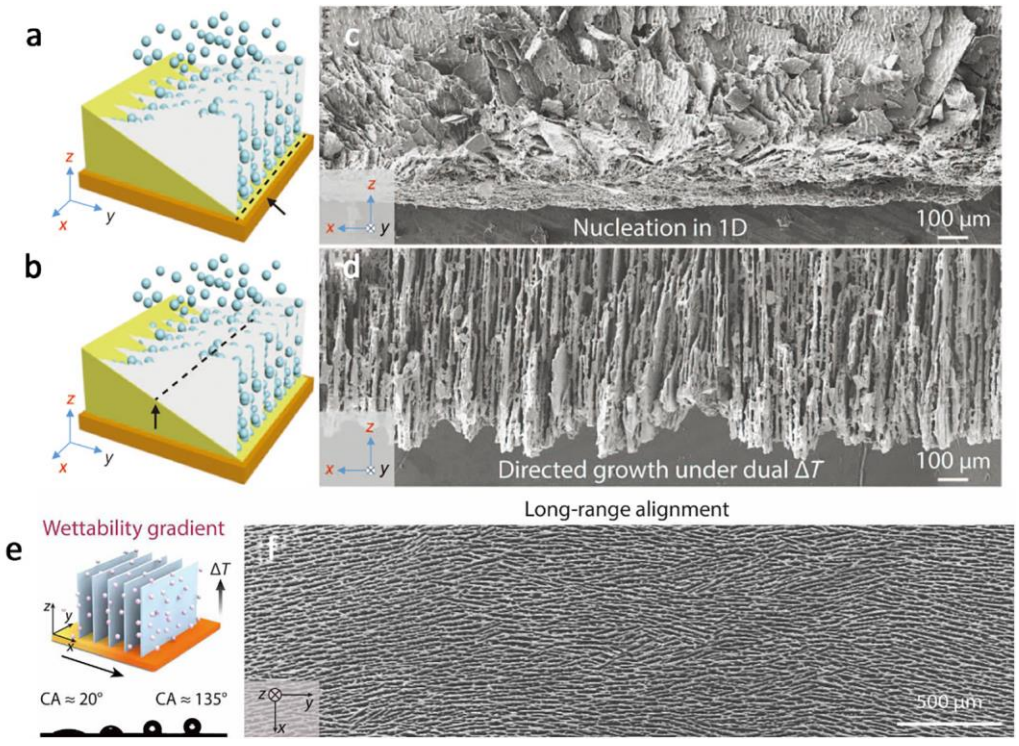

Figure 8. a,b) Schematic of the bidirectional freezing and c,d) representative SEM images of the cross sections perpendicular to the cold finger. Reproduced under terms of the CC-BY license.[61] Copyright 2015, the Authors, published by American Association for the Advancement of Science. e) Linear wettability gradient and f) orientation of long-range lamellar structure. Reproduced under terms of the CC-BY license.[8] Copyright 2020, the Authors, published by American Association for the Advancement of Science.

2.6.4. Radial freezing

Radial freezing can be categorized into introverted type (**Figure 9**a) and extroverted type (Figure 9b) by the contact surfaces between the dispersion and the cold finger. The Introverted type employs a circular mold made of copper, which controls the temperature gradient, guides ice crystal nucleation and growth, and forms radially well-aligned bioinspired structures (Figure 9c) to optimize the mechanical properties of the scaffolds.[17] Aqueous solution of sodium carboxymethyl cellulose is intuitively observed to complete freezing process in the cold finger, and pore inlet orientation and pore morphology of ice crystals after freeze-drying can be clearly seen by the naked eye. As for the Extroverted type, the cold finger is designed in the center of the round mold, and ice crystals show inside-out preferential growth, creating a thickness gradient in the radial direction.[64] We note that the obtained porous scaffold reveals the width of the lamellar spacing increases from the center to the edge. Consequently, radial freezing demonstrates more distinct variations in pore geometry and alignment of the as-prepared monoliths due to increases in interlamellar spacing, pore area, and pore wall thickness as the cooling rate decreases.

Although these two radial freezing types are both excellent processing technologies, they fail to meet the demands for the designs of biomimetic materials with functional diversity and structural complexity. Furthermore, Yin et al. fabricated a porous chitosan scaffold with radial alignment through a radial-bidirectional freezing strategy (Figure 9d).[66] The scaffold exhibited an anisotropic multidomain structure and highly radially-aligned lamellar porous, which were confirmed in the transverse cross-section (Figure 9e). Undoubtedly, the microstructure and rheological behavior of spontaneous capillary generated from interconnected gradient channels of radial-bidirectional freezing that has been put forward to manufacture more sophisticated architectures is more popular than radial freezing.

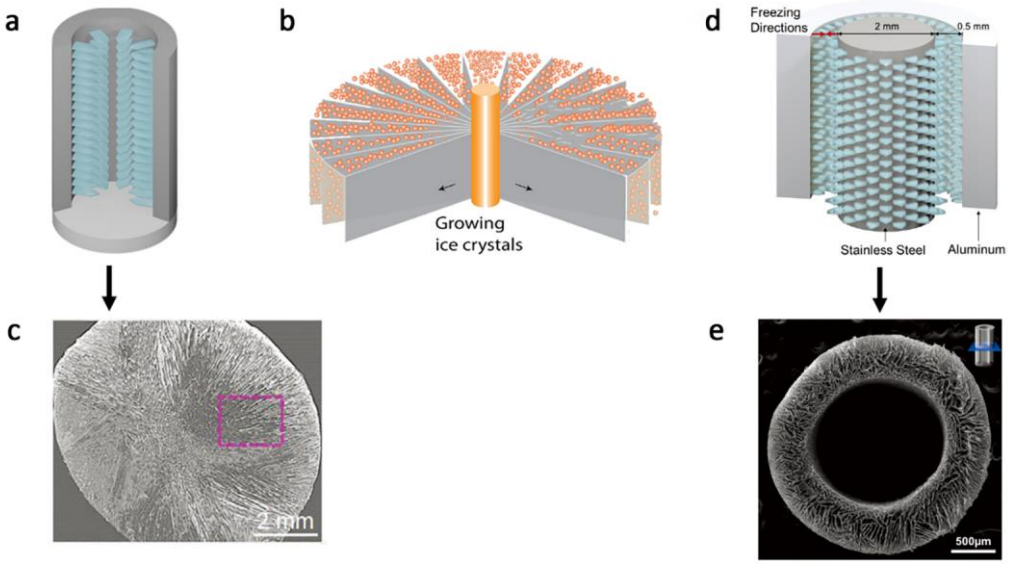

Figure 9. a) Schematic of the introverted type of radial freezing. Reproduced with permission.[16] Copyright 2019, Elsevier. b) Schematic of the extroverted type of radial freezing. Reproduced with permission.[65] Copyright 2015, Elsevier. c) SEM image of a microstructure of the introverted type. Reproduced with permission.[17] Copyright 2021, Wiley-VCH. d) Schematic of the radial, bidirectional freezing and e) SEM image of transverse cross-section. Reproduced with permission.[66] Copyright 2019, Elsevier.

3. Integrative ice frozen assembly

Ice-templating can only generate simple pore geometry by tailoring the interaction between ice crystals and the matrix but is unable to precisely control complicated macrostructures, which calls for further development of suitable technologies.[11] Combined with other materials' processing technologies (spinning, spraying, filtration, and hydrothermal), ice-templating achieves the control of microstructure (pore size, porosity, and connectivity) and macromorphology (0D sphere, 1D fiber, 2D film, and 3D monolith) to attain a balance of precise structural control, scalability, and cost–effectiveness, which are all important for constructing a more complex and hierarchical aligned structure of porous materials. Some porous materials with large specific surface area, rational porosity distribution, various surface chemical composition, and high conductivity have been fabricated up to now by ice-templating in combination with different materials' processing technologies, which contribute to facilitating the electrolyte ion/mass transport, the rich surface active sites, and the effective stress buffering.

3.1. Spray-freezing

Spray-freezing is a versatile technique able to make microstructure controllable and extensibility.[28,67,68] It is frequently used for the directional control of colloidal particles to create radial lamellar microporous networks, conducive to forming high-energy-density porous materials via dense assembly (**Figure 10**). In view of the above, fine-tuning the physical interaction and chemical composition of hybrid materials is crucial to achieving superior scaffolds, which helps accurately tailor the pore geometry, pore size distribution, and pore connectivity of the final scaffold structure and thereby makes it easier to comprehend the benefits of materials for energy storage and conversion.

Spray–freezing consists of spraying and ice-templating to control multiple compositions and uniform distribution. The dispersion is quickly sprayed as droplets into a coagulation bath by using an electric nozzle/needle tube. Ice crystals grow in the liquid particles from outside to inside, maintaining the spherical structure, and freeze-drying is performed to prevent the collapse of the porous structure due to excessive blocking or particle aggregation, after which interconnected open-porous structures are formed.[68,69] To achieve accurate regulation of porous materials, Nakhanivej et al. integrated electrospray frozen assembly with a tip sonication process to fabricate high-performance LIB cathode with vanadium pentoxide (V_2O_5) and reduced graphene oxide (rGO) as hybrid materials (Figure 10a–b).[70] The surface of the resulting composite microspheres was coated with V_2O_5 particles, which effectively relieved the internal stress of the microspheres and further enhanced the conductivity of the porous material. Furthermore, the radial porous structure derived from V_2O_5 particles mixed with rGO was also conducive to rapid lithium ion diffusion and improved the rate performance of V_2O_5/rGO composite microspheres (Figure 10c). Meanwhile, hierarchically open-porous microspheres assembled by spray-freezing enables to open spaces for the redox sites onto the surface of spherical particles and to short diffusion pathway for ions and electrons from the surface to the core. He et al. prepared Pt-modified graphene aerogel microspheres (Pt/rGOAMs) by integrating electrospraying, freeze-casting, and solvothermal process (Figure 10d,e).[71] Compared with Pt/C and Pt/GO as catalysts, Pt/rGOAMs exhibited superior electrocatalytic activity toward methanol oxidation (Figure 10f). This was mainly contributed by the center-diverging microchannels in the microspheres, which were favorable for the uniform dispersion, embedding, and aggregation of Pt particles therein. The results of the studies confirmed that varying the nature and concentration of dispersion, and the diameters of nozzle triggers a more the controllability and versatility of spray-freezing.

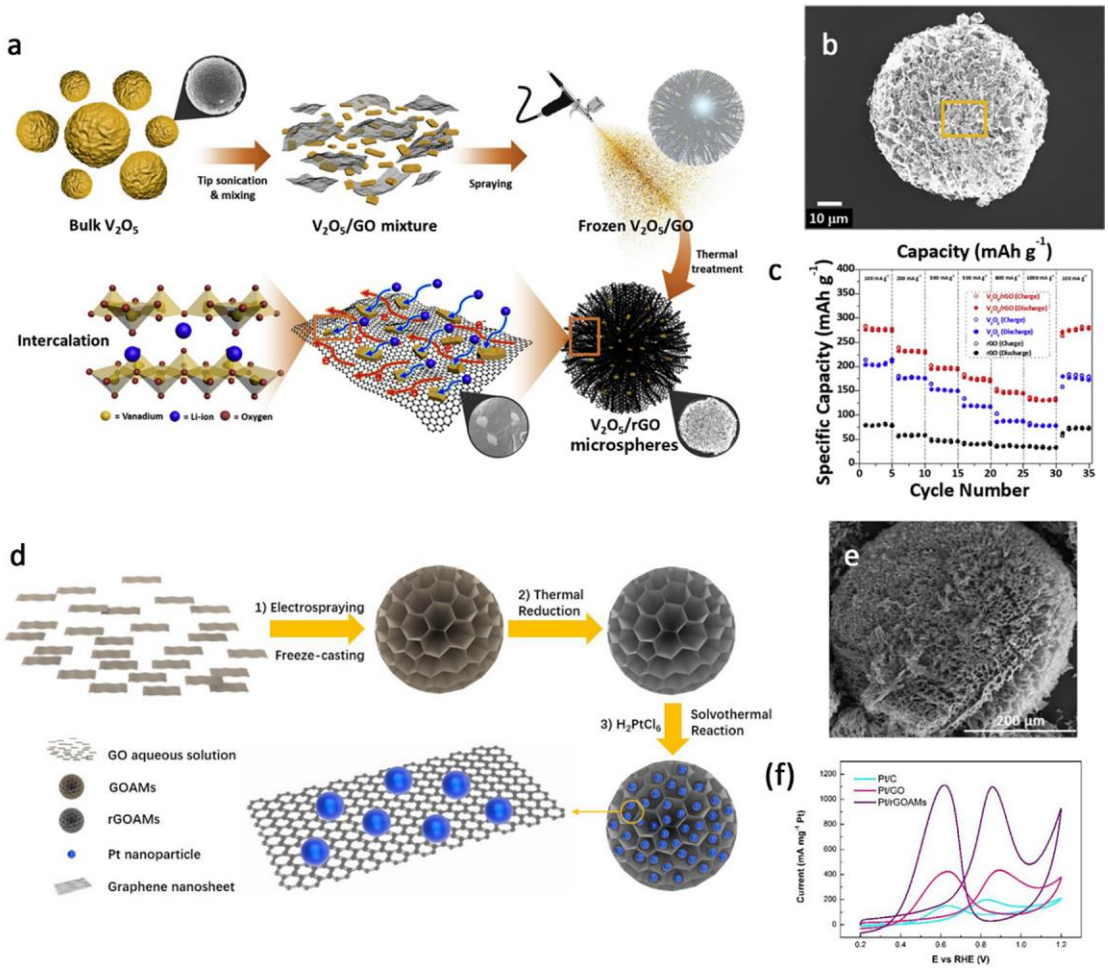

Figure 10. a) Schematic illustration of fabricating V_2O_5/rGO composite. b) SEM image of V_2O_5/rGO composite. c) Rate capabilities of various composites at different current densities. Reproduced with permission.[70] Copyright 2019, Elsevier. d) Schematic illustration of synthesizing Pt/rGOAMs. e) SEM image of Pt/rGOAMs. f) CV of different composite materials at a scan rate of 50 mV s^{-1}. Reproduced with permission.[71] Copyright 2019, American Chemical Society.

3.2. Freeze-spinning

Spinning is a generic technique that can derive interlinked structures to create lamellar interconnected macroporous networks applicable in various fields, attracting much attention because of the low density, versatility, and high aspect ratio of the resulting materials (**Figure 11**a).[72–74] However, the final scaffold structures are constrained in some aspects (open porosity, pore diameter, pore geometry, and desired thickness), which results in the degraded mechanical properties of materials.[75–77] In addition, 3D hierarchical network structures are equally crucial since porous structures are helpful for electrolyte ion/electron transport to improve electrochemical performance. For that, the flexible and cost-effective strategy of combining ice frozen assembly and electrospinning can fabricate composite porous materials with adjustable porosity and different geometric shapes by utilizing suitable materials to cope with low energy density and inferior magnification performance. Moreover, integrative ice frozen assembly gives full play to the inherent advantages of the processing technologies, i.e., the large specific surface area, high aspect ratio, and superior topological structure of the resulting materials (Figure 11b).

The basic procedure of freeze-electrospinning is as follows: some inorganic or organic components are made into electrospun fibrous mats with the help of an electrospinning nozzle; they are dissolved in a non-solvent medium to form a dispersed slurry of fibers; the network structure is reassembled under low-temperature freezing; freeze-

drying is performed to prepare 3D lamellar macrostructures.[71,78,79] Freeze-spinning can readily tailor pore morphology of various composites from micro to macro structures, which affects specific surface area, mechanical strength, and tap density. The theoretical analysis is substantiated by orderly porous structures on the improved electrochemical performance through facilitating ion/mass transport. With this finding, Cui et al. established the axial-alignment pore geometry of silk fibroin fibers by freeze-electrospinning (Figure 11c) and made significant progress in improving electrochemical performance.[80,81] As the pore diameter became larger, the average tensile strength and average elongation of the fibers increased first and then decreased, which indicated that the surface area and porosity of the scaffold were significantly enhanced by ice freezing (Figure 11d). In another study, Xu et al. fabricated a special core–shell structure of reduced graphene porous fibers (RGPFs) and a well-aligned network structure to achieve low density and great conductivity by using the freeze spinning technology (Figure 11e,f).[82] Therefore, it is demonstrated that freeze-(electro)spinning has the advantages of controllability, easy processing, and versatility. Various hierarchical lamellar porous structures can be assembled for thermal management and energy storage by varying influencing parameters (such as the inherent characteristics of the liquid, process, environmental parameters, the type of spinneret, and the geometry of the collector).

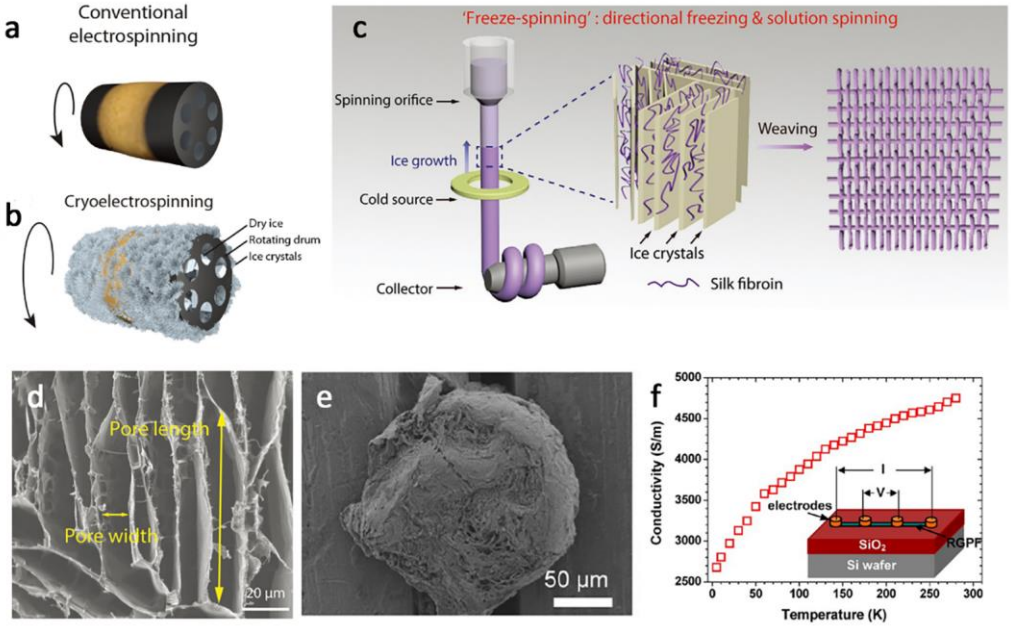

Figure 11. Formation of different network structures by a) conventional electrospinning and b) cryoelectrospinning. Reproduced with permission.[83] Copyright 2016, Wiley-VCH. c) Schematic illustration and d) SEM image of the freeze-spinning technique. Reproduced with permission.[81] Copyright 2018, Wiley-VCH. e) SEM image of the core–shell structure of RGPFs and f) conductivity curve of annealed RGPFs as a function of temperature. Reproduced with permission.[82] Copyright 2012, American Chemical Society.

3.3. Ice-templating combined with filtration

Researchers have attempted to employ vacuum filtration for achieving hierarchical lamellar porous structures with unique anisotropy and stable energy storage capability in hope of making them become candidates in scaffold fabrication.[84–86] However, the materials prepared by this method cannot maintain a stable structure, which leads to interference with electrolyte ion/electron tranport and less effective stress buffering. In response, vacuum filtration is integrated with ice-templating to create scaffolds with superior multi-dimensional lamellar macrostructures for wearable electronics, energy storage and conversion, and highly insulating fabrics.[28,87–89]

In the above-mentioned integrative strategy, vacuum filtration is utilized to regulate and assemble the structure

of dispersed materials, and then controlled crystallization by ice-templating are conducted to induce the Randomly dispersed materials for fabricating an orderly lamellar porous structure. It is this method to prepare a unique anisotropic structure that porous materials have the benefits of large specific surface area and structural stability. With partially reduced graphene oxide (GO) microgels derived from pre-reduction, Shao et al. efficiently synthesized a dense lamellar porous graphene film via ice-templating followed by filtration assembly (**Figure 12**a–e).[90] Especially, the solidification dynamics of the freezing process and the porous structure formation changed, preventing the stacking between layers and promoting the diffusion of electrolyte ion/electron (Figure 12f). The 3D porous rGO sheets exhibited an ultra-high mass capacitance of 284.2 F g^{-1} at a current density of 1 A g^{-1}, and the 3D porous rGO films exhibited higher capacitance retention (97.6%) than rGO films over 10 000 charge/discharge cycles at a current density of 25 A g^{-1}, showing excellent durability (Figure 12g,h). This demonstrated that its features are the lamellar structure of composites through surface tension modification with nanoparticles and to achieve porous channels in between the layers. Xu et al. prepared N-rich holey rGO films (N-HRGO) via H_2O_2-assisted etching followed by modified vacuum filtration and freeze-casting.[91] The vertically arranged hierarchical porous structure of N-HRGO provided fast electrolyte ions/electrons transport, rich surface active sites, and effective stress buffering (Figure 12i–k). N-HRGO still maintained superior cycling stability and coulombic efficiency after 5000 cycles at 2 A g^{-1} (Figure 12l). In particular, this method can be extended further to construct porous structures of functional nanomaterials for energy storage and conversion applications.

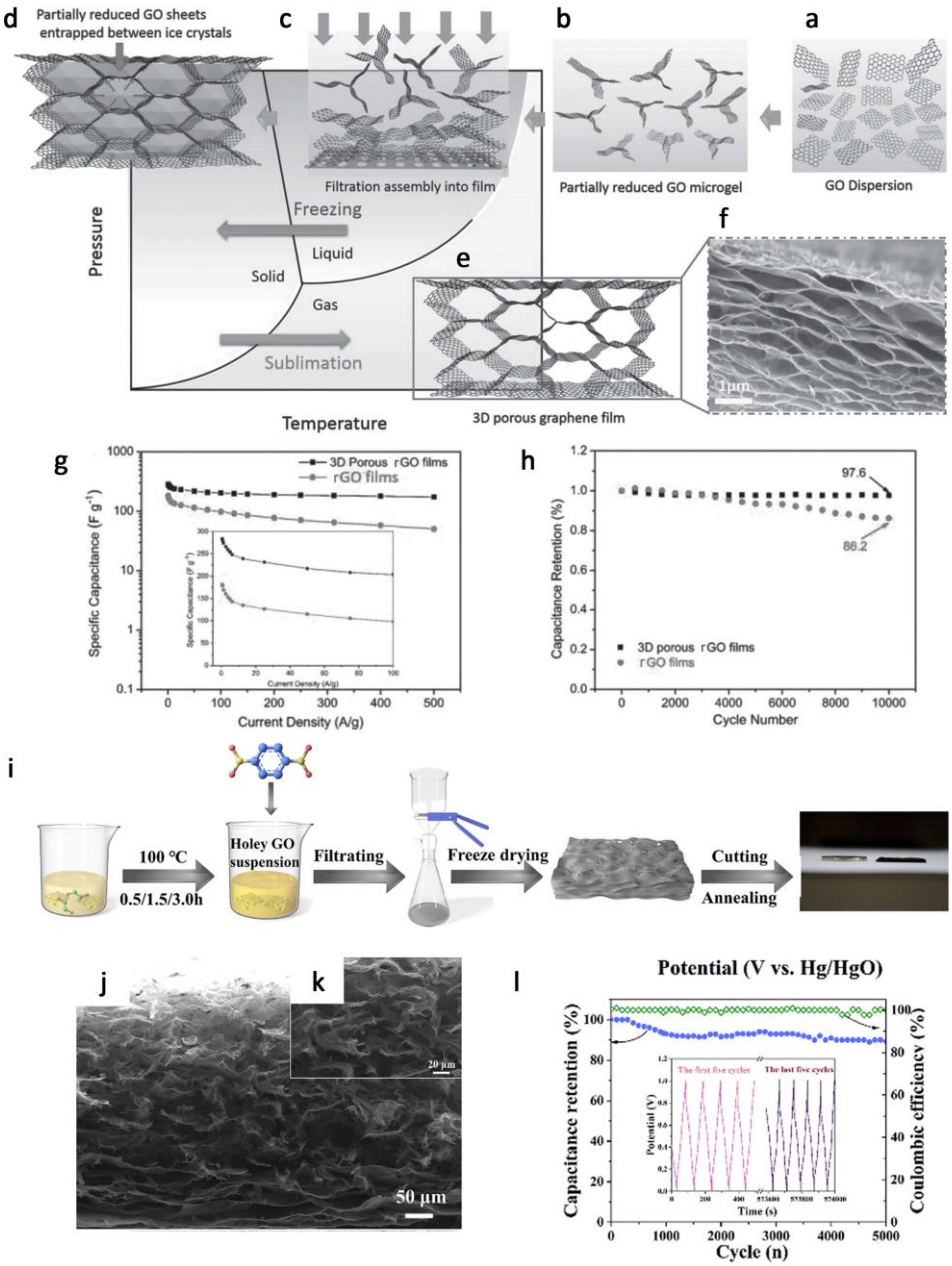

Figure 12. a–e) Schematic illustration of forming a 3D porous graphene film. f) Typical cross-section SEM image of the 3D porous graphene film. g) Cycling stability and h) specific capacitances of 3D porous rGO films and rGO films. Reproduced with permission.[90] Copyright 2016, Wiley-VCH. i) Schematic illustration of fabricating the N-rich porous graphene film. j,k) Cross-section SEM images of the N-rich porous graphene film. l) Cycling stability at a scan rate of 2 A g^{-1}. Reproduced with permission.[91] Copyright 2021, Elsevier.

3.4. Integrating ice-templating with hydrothermal

The hydrothermal method is a simple and mild technology for preparing lamellar structures with a large specific surface area, which support rapid ion/electron diffusion and are stable in energy storage. Although porous materials can be constructed by the hydrothermal method, some defects limit its applications. For example, it cannot accurately regulate the inner morphology of the scaffold structure, which significantly degrades the performance of the composite materials.[92–94] Therefore, the combination of hydrothermal and ice freezing is exploited to construct to build multi-dimensional network macrostructures.

Integrating hydrothermal method with ice-templating is to construct the scattered assemblies for directing the chaotic structure to form the ultimate orientated porous structure. For instance, Zhao et al. employed GO-assisted hydrothermal process and ice-templating to construct a 3D $Ti_3C_2T_x$ MXene/rGO hybrid aerogel (MGA) with excellent electrical conductivity, which can be used to build a 3D macrostructure for energy applications (**Figure 13**a,b).[95] The porous structure of the hybrid aerogel endowed the epoxy nanocomposite with conductivity up to 695.9 S m^{-1}, which was conducive to the rapid charging and discharging of the porous material (Figure 13c). The multifunctional carbon fiber of the porous materials, emerging ten to hundreds of microns in length, could be constructed through this method. Another example is the development of structures for thermal management. Lin et al. constructed a 3D spider-web-like (sw) graphene skeleton (GS) via hydrothermal reduction and freeze-casting, which were followed by vacuum impregnation in paraffin wax (PW) to manufacture thermally conductive phase change composites (sw-GS/PW).[96] The graphene-based network structure had high cross-plane and excellent shape stability, showing the potential for effective thermal management of SCs and LIBs (Figure 13d). Additionally, this material is promising for emerging applications such as biomedical devices and flexible scaffolds to construct multidimensional architectures by the integration of hydrothermal and ice freezing owing to the rich surface-exposed active sites, the fast charge/ion diffusion pathways, and the flexible features for wearable, stretchable, and flexible devices.

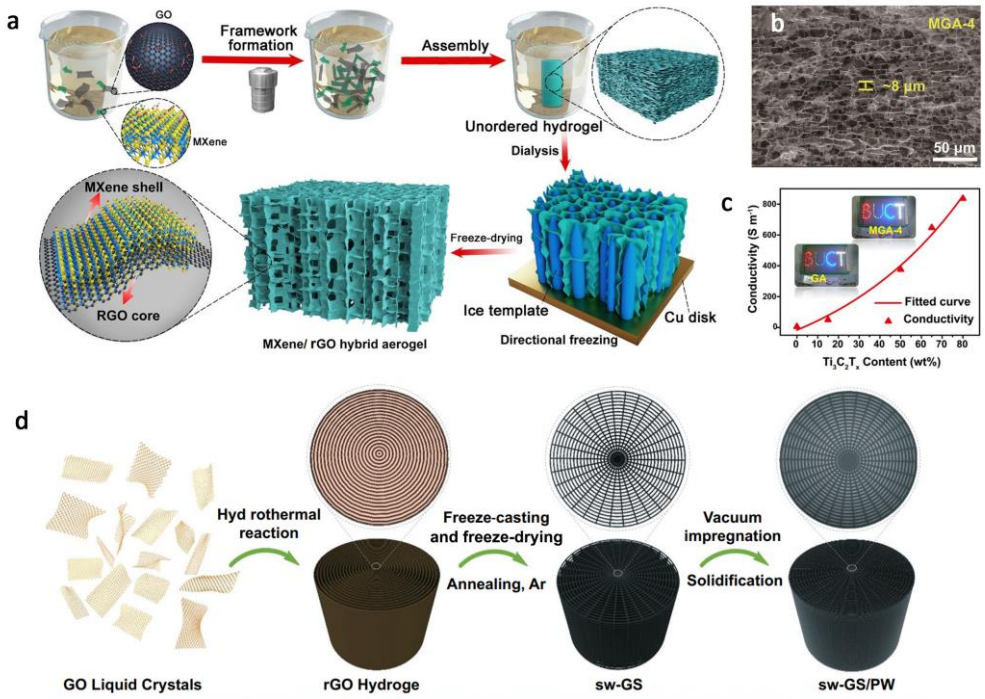

Figure 13. a) Schematic illustration of fabricating a $Ti_3C_2T_x$ MXene/rGO hybrid aerogel. b) SEM image of the hybrid aerogel. c) Relationship between $Ti_3C_2T_x$ content and MGA conductivity. Reproduced with permission.[95] Copyright 2018, American Chemical Society. d) Schematic illustration of fabricating sw-GS/PW composite. Reproduced with permission.[96] Copyright 2021, Springer Nature.

4. Energy storage and conversion devices

Currently, higher requirements are put forward for renewable energy storage as well as supplement in accordance with demand. The rational design of functional nanomaterials has been extensively investigated to pave the way for enhancing energy storage and conversion devices.[70,97–100] The geometric characteristics of porous materials play a significant role in demonstrating both outstanding electrochemical performance and excellent structural stability in terms of the specific surface area, the pore volume, and the pore size distribution.[11,44,101] For exerting the synergistic

effect of monomer materials on the stabilization of electrochemical performance, it is necessary to develop an assembling method for the as-designed functional nanomaterials that enables the morphology and dimension of the hierarchical architecture to be precisely controlled for optimizing charge transfer, ion/mass transport. Integrative ice frozen assembly is considered a highly efficient technology to control the inner microstructure and outer macromorphology, which is favorable for preparing porous materials with high energy density, high power density, and strong tolerance (**Table 1**).

Table 1. Texture characteristics of porous structural materials prepared via ice-templating combined with different materials' processing technologies.

Material	Method	Structure	Specific surface area / (m^2 g^{-1})	Pore volume / (cm^3 g^{-1})	Pore size distribution / (nm)	Capacitance/ Capacity	Retention on cycling	Type of devices
Fe_3O_4/rGO[66]	Electrospraying, ice freezing	Hierarchical open-porous spherical structure	313.6	0.776	10–100	1069.7 mAh g^{-1} at 0.1 A g^{-1}	74.6% after 300 cycles	LIB (anode)
V_2O_5/rGO[102]	Electrospraying, ice freezing	Hierarchical open-porous microball	38.18	0.20	2–40	273 mAh g^{-1} at 0.1 A g^{-1}	80.4% after 200 cycles	LIB (anode)
FeOOH/egg plant-derived carbon tube network (ECTN)[103]	Hydrothermal, ice freezing	Nanorod-like super-long carbon tube network structure	303	0.24	2–10	396 F g^{-1} at 0.5 A g^{-1}	83% after 500 cycles	SC
CNF/CCS/ PANI[104]	Vacuum filtration, freeze-drying	Hierarchical strapped network structure	20.9	0.05	10.5–16.7	220 F g^{-1} at 1 mA cm^{-2}	83% after 3000 cycles	SC
$NiCoO_2$/rGO[105]	Filtration assembly, freeze-casting, thermal treatment	Hierarchical honeycomb-like network	111.31	0.34	2–20	-	-	Fuel cell
Cellulose/ $NH_4H_2PO_4$[106]	Directed freeze-casting, dual-activation	Hierarchical aligned porous tubular structure	1553	0.81	2–10	367 F g^{-1} at 1.0 A g^{-1}	95% after 5000 cycles	SC
Biomass sorghum vinasse[107]	High-energy ball milling treatment, ice freezing	Highly porous nanoplatelet microstructure	3047	1.35	0.7–4.0	329 F g^{-1} at 1.0 A g^{-1}	88% after 10 000 cycles	SC
Multiwall carbon nanotube (MWCNT)/γ-Fe_2O_3[45]	Ozonation, ice-templating, and thermal treatment	Spider-web-like structure	449.2	1.05	3.77–100	822 mAh g^{-1} at 0.1 A g^{-1}	≈88% after 310 cycles	LIB (anode)

4.1. Supercapacitor

SCs are electrochemical energy storage devices with a high specific capacity, long cycle life, fast charge/discharge capability, and high coulombic efficiency.[108,109] They can be classified by the mechanism of energy storage as

electrochemical double-layer capacitors (EDLCs) and pseudocapacitors (PCs). However, the ion-confinement effect of double-layer capacitance as well as surface characteristics of the electrode materials, which limits energy density of EDLCs.[110,111] In addition, PCs have higher energy density due to their unique structure and tunable surface chemical properties, which does not affect the charge storage capacity, whereas the instability of the reversible electrochemical reaction of PCs could impede electron transmission and lower rate capability.[112] Improving material structural integrity, electrical properties, and electrochemical behavior ought to be prioritized to alleviate the limitations of EDLCs- and PCs-based materials. Thus, it is essential to construct a freestanding SCs electrode through integrative ice frozen assembly.

Graphene, among of the carbon materials, is one of the critical materials to the greatly improved electrochemical performances of SCs electrodes due to it being large specific surface area, tailorable structure, excellent conductivity, and a broad potential window.[113] For instance, Deng et al. designed holey GO (HGO) clinging to the $Ni(OH)_2$@NF backbone via a one-pot hydrothermal strategy and induced GO to infiltrate into the backbone by ice-templating, thereby constructing an asymmetric solid-state capacitor (ASC) (**Figure 14**a).[114] The porous structure was designed to have a long-range orderly lamellar graphene scaffold, which means that it had a hollow microstructure and flexibility (Figure 14b,c). At the same time, the galvanostatic charge–discharge (GCD) curve did not change significantly at the beginning and the end of cycling. As rHGO/NiO fell off the backbone and was captured by rGO, the area-specific capacitance first decreased, then increased, and finally decreased with the increase in cycling number, indicative of the cycling stability and excellent electrochemical performance of the ASC setup (Figure 14d). Because of features, such as excellent conductivity, high pseudo-capacitance, tailorable wettability, and superior rate capability, carbon materials with heteroatoms doping deservedly have received considerable attention.[115-116] For the development of the high-performance SCs, many efforts have been ever-growingly insights into the heteroatoms (e.g., N, P, B, S, transition metals) doping into graphene. Liang et al. had reported to prepare N-doped porous carbon nanosheets (NPCNs) and realized their assembly into 3D superstructure by integrating ultrasonic atomization technology with ice-templating, which were respectively responsible for atomizing poly(amic acid) ammonium salt (PAS) into micron droplets and freezing (Figure 14e).[117] As shown in Figure 14f, the seaweed-like hierarchical structure of NPCNs was beneficial to controlling the stacking of carbon nanosheets. Simultaneously, the high specific surface area (833 $m^2\ g^{-1}$) and large interlayer spacing (0.38 nm) of NPCNs provided convenience for the increases in surface active sites and electrolyte ion/mass diffusion channels, endowing the electrode materials with an excellent energy density (4.7 Wh kg^{-1} at 0.5 A g^{-1}) and outstanding cycling stability (about 98% capacity retention at 1.0 A g^{-1} after 10 000 cycles) (Figure 14g). The generally well-known transition metal oxide has been ever-growing interest as a candidate for SCs electrode materials as it is associated with excellent specific energy. However, there is still much room for improvement in the cycling stability and electrical conductivity. For that, combining transition metal oxide with carbon materials facilitates more effective advancements in the synthesis and design of materials because of the synergistic enhancement effects. Bhattacharya et al. demonstrated a generic way to uniformly assemble dispersed $CoSO_4 \cdot 7H_2O$ on the inner and outer surfaces of GO by sonication and obtained CoO/GO after ozone treatment for oxidizing the mixture.[118] After that, the composite underwent directional freezing via ice-templating, and annealed CoO/GO was reduced to form CoO/rGO (Figure 14h). The transmission electron microscope (TEM) image of the sample showed a 3D network structure, with CoO nanoparticles evenly distributed in the GO matrix (Figure 14i). The CoO/rGO composites had specific surface area of 57.5 $m^2\ g^{-1}$ and a high specific capacitance of up to 239.4 F g^{-1}. Figure 14j reflects that the electrode material still retained 93.2% of cycling stability after 10 000 cycles.

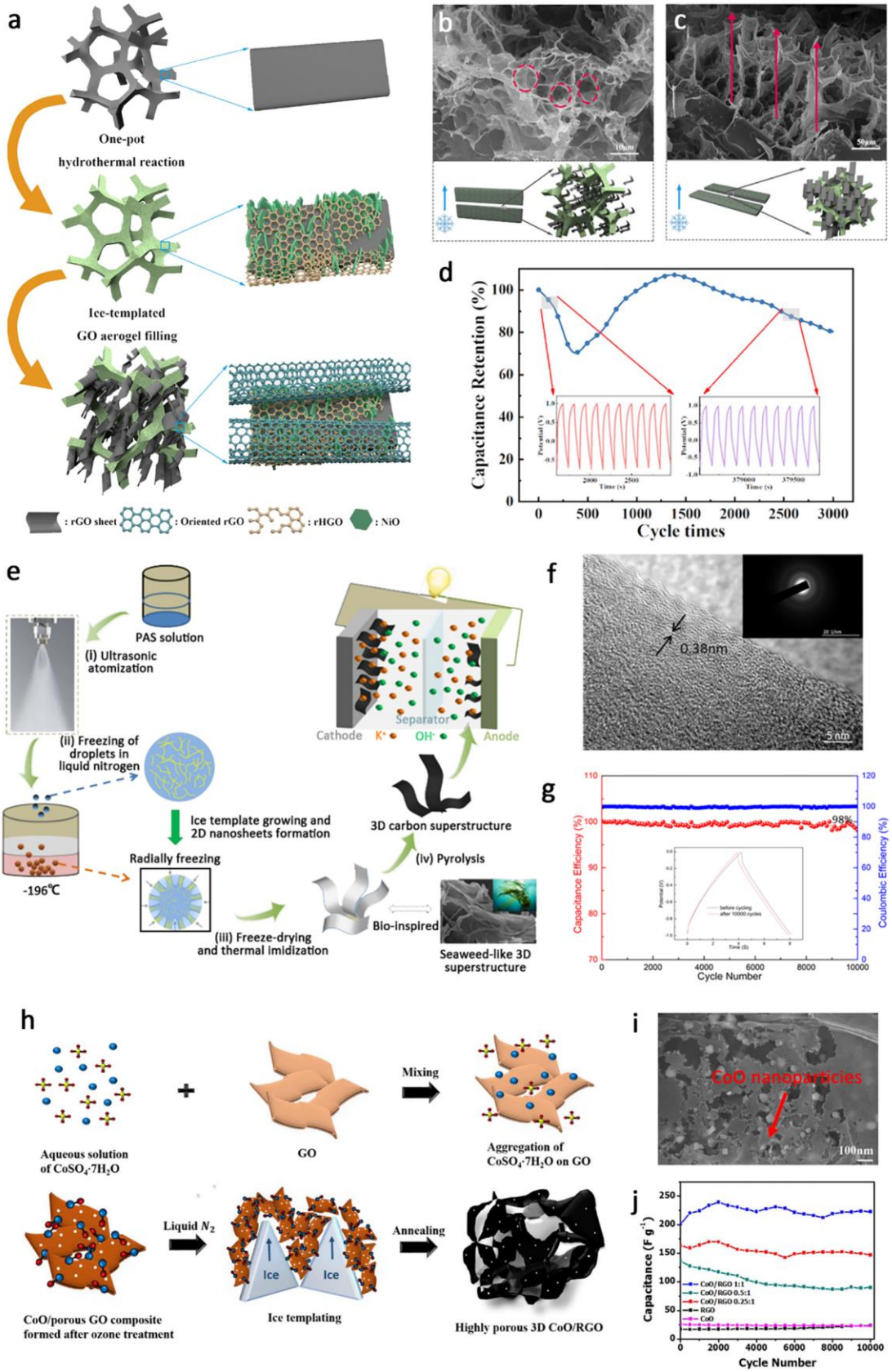

Figure 14. a) Schematic illustration of fabricating hybrid electrode materials with different freezing directions. b,c) SEM images of the hybrid electrode materials. d) Cycling curve in ASC setup. Reproduced with permission.[114] Copyright 2022, Elsevier. e) Schematic illustration of fabricating NPCNs. f) TEM image of NPCNs. g) Cycling stability test on NPCNs at 10 A g^{-1} for 10 000

cycles. Reproduced with permission.[117] Copyright 2022, American Chemical Society. h) Schematic illustration of fabricating CoO/RGO nanocomposite. i) Field emission SEM (FESEM) images of CoO/RGO nanocomposite. j) Cycling stability (10 000 cycles at 10 A g^{-1}) of CoO/RGO nanocomposite. Reproduced with permission.[118] Copyright 2018, Elsevier.

4.2. Lithium-ion battery

LIBs are a kind of popular power source for portable electronics, electric cars, long-term energy storage, etc. due to their excellent cycling performance and high charge and discharge efficiency.[119,120] However, their wider applications are hindered by such drawbacks as low battery capacity, short service life, and high-voltage polarization caused by the slow diffusion of lithium ions between the positive and negative electrodes.[121,122] Researchers have taken measures to overcome these deficiencies, including introducing carbon as a buffer, utilizing the prelithiation technology, and adopting battery thermal management systems (BTMSs), which help boost the performance of LIBs in energy storage and conversion. Integrative ice frozen assembly has drawn increasing attention as a simple and effective technology due to its ability to control the orientation in tailoring the microstructure and macromorphology of LIBs. Hierarchical porous electrode materials with long-term cycling stability and excellent rate performance have been developed by the technology, which is sustainable with respect to efficient active sites for lithium-ion intercalation-deintercalation behaviors and storage.[123,124]

Recently, improving lithium ions diffusion pathways and tuning vertically aligned structures are significant methods to greatly reinforcement of electrochemical performances in the energy storage and conversion field. Yun et al. conducted integrative spray-frozen assembly to form hierarchical porous microspheres (hpMSs) composed of Fe_3O_4 and rGO, during which the droplets of the sprayed dispersion were rapidly frozen by liquid nitrogen to construct radially arranged microstructure (**Figure 15**a,b).[68] The porous structure and spherical morphology, and constituent composition of the hierarchical architecture unchanged in the thermal annealing stage were beneficial for shortening the electrolyte ion/electron diffusion pathways and increasing the surface-exposed active sites, indicating the excellent specific capacity (1069.7 mAh g^{-1} at 0.1 A g^{-1}) and cycling stability of hpMSs, resulting in significantly sought-after than those of samples with the same composition and different morphologies (Figure 15c). Due to the relatively lower capacity of cathode material, optimizing interconnected conductive paths and hierarchical lamellar structures of electrode could effectively improve the energy density of LIBs. For instance, Li et al. reported a strategy to fabricate a cathode material ($Li[Li_{0.2}Ni_{0.2}Mn_{0.6}]O_2$) with a hierarchical micro/nano-structure, namely the extrusion of carbonate precursor ($Ni_{0.2}Mn_{0.6}(CO_3)_{0.8}$) via ice-templating combined co-precipitation (Figure 15d).[125] The homogeneous distribution of nanoparticles was observed in the microspheres, which was attributed to suppressing the agglomeration of nanoparticles by freeze-drying and resulted in an excellent mesoporous structure of the Li-rich material (Figure 15e). Its discharge capacity was 280.1 mAh g^{-1} at 0.1 C and was stable over 50 cycles at 5 C with a capacity retention of 82.1% (Figure 15f). At present, developing flexible LIBs still face some challenges associated with balancing the electrochemical performance and mechanical flexibility of electrode materials, thereby deteriorating cyclic stability, energy density, and coulombic efficiency. In order to meet the requirements of practical applications, Li et al. designed a dual conduction network structure through the 3D printing technology and printed layer by layer via directional freezing followed by freeze-drying.[126] Then filaments were induced to fabricate lithium iron phosphate/carbon nanotube/cellulose nanofiber (LFP/CNT/CNF) thick electrodes with different layers (Figure 15g). As shown in Figure 15h,i, the LFP/CNT/CNF with a disordered network structure was fabricated via undirectional freezing. In addition, it is noteworthy that the thick electrode with high mechanical reinforcement prepared is desired to realize a suitable form of energy source showing a more uniform and orderly microchannel structure by directional freezing assisted 3D printing. The thick electrode exhibited superior mechanical properties under external force (bending and compression), achieving the rapid diffusion of electrons and effective stress release (Figure 15j,k). Compared with other flexible LIBs, the full battery with an 8-layer electrode indicated a high energy

density (15.2 mWh cm^{-2}) at a current density of 0.2 C and excellent power density (75.9 mW cm^{-2}) at 5 C.

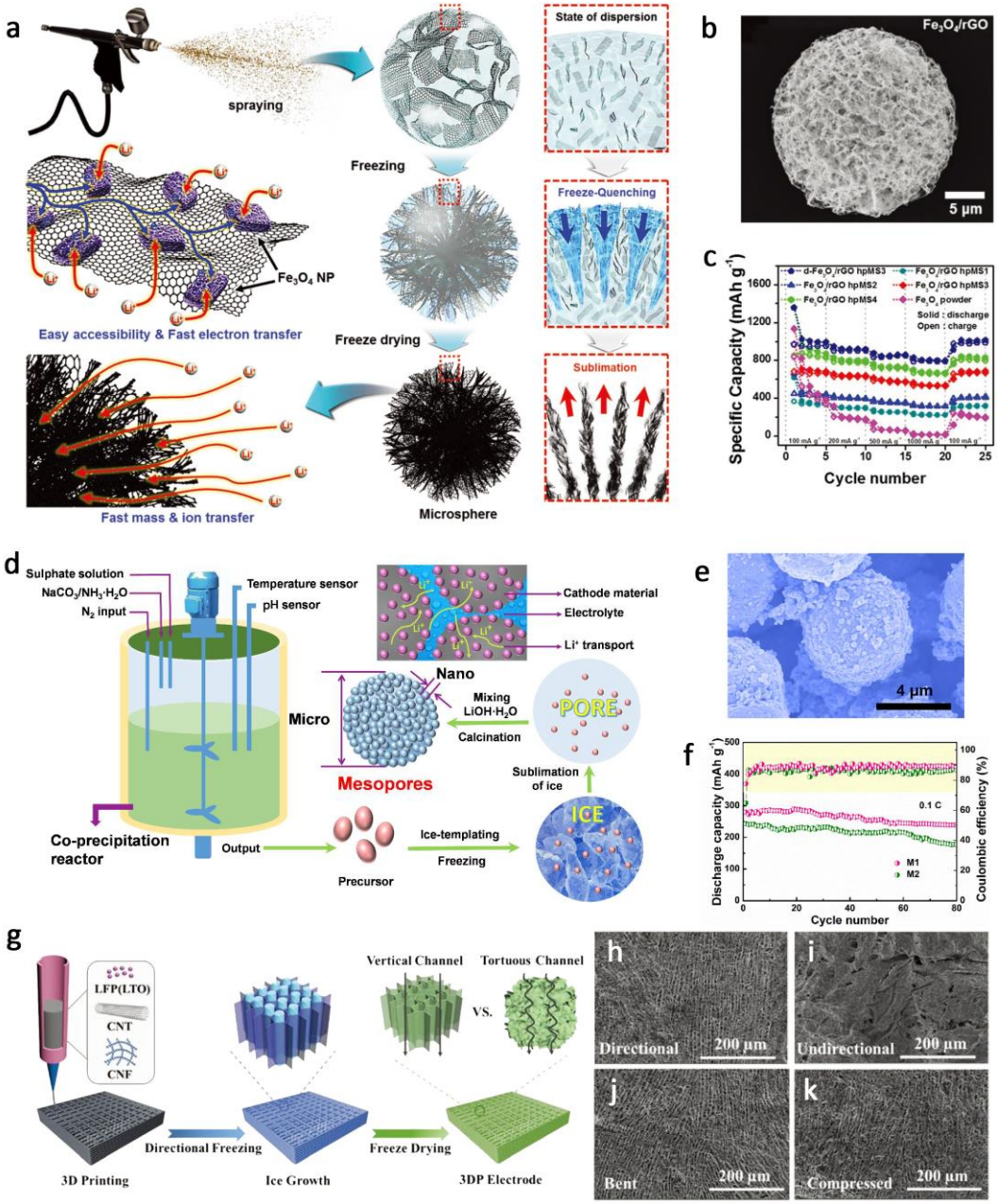

Figure 15. a) Schematic illustration of fabricating Fe_3O_4/rGO hpMSs and b) their SEM image. c) Rate performance of Fe_3O_4/rGO hpMSs at different current densities. Reproduced with permission.[68] Copyright 2019, Wiley-VCH. d) Schematic illustration of fabricating Li-rich electrode material. e) SEM image and f) cycling stability of the Li-rich electrode material. Reproduced with permission.[125] Copyright 2016, American Chemical Society. g) Schematic illustration of fabricating LFP/CNT/CNF thick electrode. SEM images of freezing printed LFP/CNT/CNF electrodes by h) directional freezing, i) conventional freezing, after j) bending, and k) compressing. Reproduced with permission.[126] Copyright 2022, Wiley-VCH.

4.3. Solar-driven steam generator

Solar-driven steam generation is a promising and sustainable technology that converts solar energy into heat energy to evaporate water, after which fresh water can be collected by lowering the steam temperature.[127–129] Currently, there are still some limitations in designing the scaffold structures, which result in low thermal conversion efficiency,

functional stability, and scalability.[130] These drawbacks make it a necessity to incorporate the morphology and characteristics of structures to bridge theoretical and empirical work on thermal power conversion and moisture transport.[129] Integrative ice frozen assembly has generally been employed to construct solar-driven steam generators due to its capacity in the fabrication of materials with a radial structure, which can tailor the pore sizes of the materials to the submicrometer level. In addition, the vertically aligned porous structure in the optimal design and the consequent production of the capillary effect further facilitate water absorption/transport, resulting in improved heat conversion efficiency of solar energy.

Nanostructured carbon materials are penetrating into the field of solar-driven steam generation through constructing an effective water-cycling system made up of vertically aligned bilayer-channel architectures. Xu et al. designed a bilayer polyacrylamide (PAAm) aerogel with radially aligned channels by using ice-templating to regulate the radial structure of the scaffold and in-situ cryopolymerization under ultraviolet (UV) (**Figure 16**a).[56] The aerogel structure took advantage of the wrinkled internal surface to improve mechanical properties and the capillary effect generated by micron pores, which was conducive to the water transport capacity (Figure 16b,c). Compared with pure water, single PAAm-radial aerogel, the bilayer aerogel had superior water evaporation rate and energy efficiency during solar-driven steam generation (Figure 16d). Enlightened by tree with high-efficiency water extraction, Chen et al. prepared a pristine $Ti_3C_2T_x$ hydrogel by employing freezing-induced pre-assembly of dispersed $Ti_3C_2T_x$ and the subsequent thawing process for modification via in-situ intercalation chemistry (in proton acid) (Figure 16e).[131] The vertically aligned channels of the pristine $Ti_3C_2T_x$ hydrogel with long-range oriented microstructure could meet the requirements of rapid mass transfer (Figure 16f,g). Meanwhile, the absence of extrinsic gelators and the highly anisotropic microstructure contributed to superior mechanical properties and conductivity of the pristine $Ti_3C_2T_x$ hydrogel for achieving an excellent performance (1.90 kg m^{-2} h^{-1} under 1 kW m^{-1} radiation) in solar-driven steam generation so that thermal dissipation can be suppressed (Figure 16h). In order to overcome the bottlenecks of carbon-based absorbers with high cost and low internal light-to-heat conversion efficiency, the conductive polymer exhibits effective potential that the strong affinity of coating on the carbon-based material. For instance, Li et al. developed a spray-freezing strategy to fabricate assembled spherical carbon (ASC) materials by regulating the concentration of the phenolic resin solution (Figure 16i,j).[132] Finally, the solar-driven steam generator with high receiver efficiency (83.6%) and evaporation rate (1.343 kg m^{-2} h^{-1}) under one sun illumination was prepared by combining polyurethane foam (PU) as matrix and ASC (Figure 16k,l). More importantly, these biomimetic designs with the superiority of water-transporting channels and large contact interfaces can offer theoretical guidance not only for designing solar-driven steam generation but also for constructing other kinds of energy storage and conversion devices.

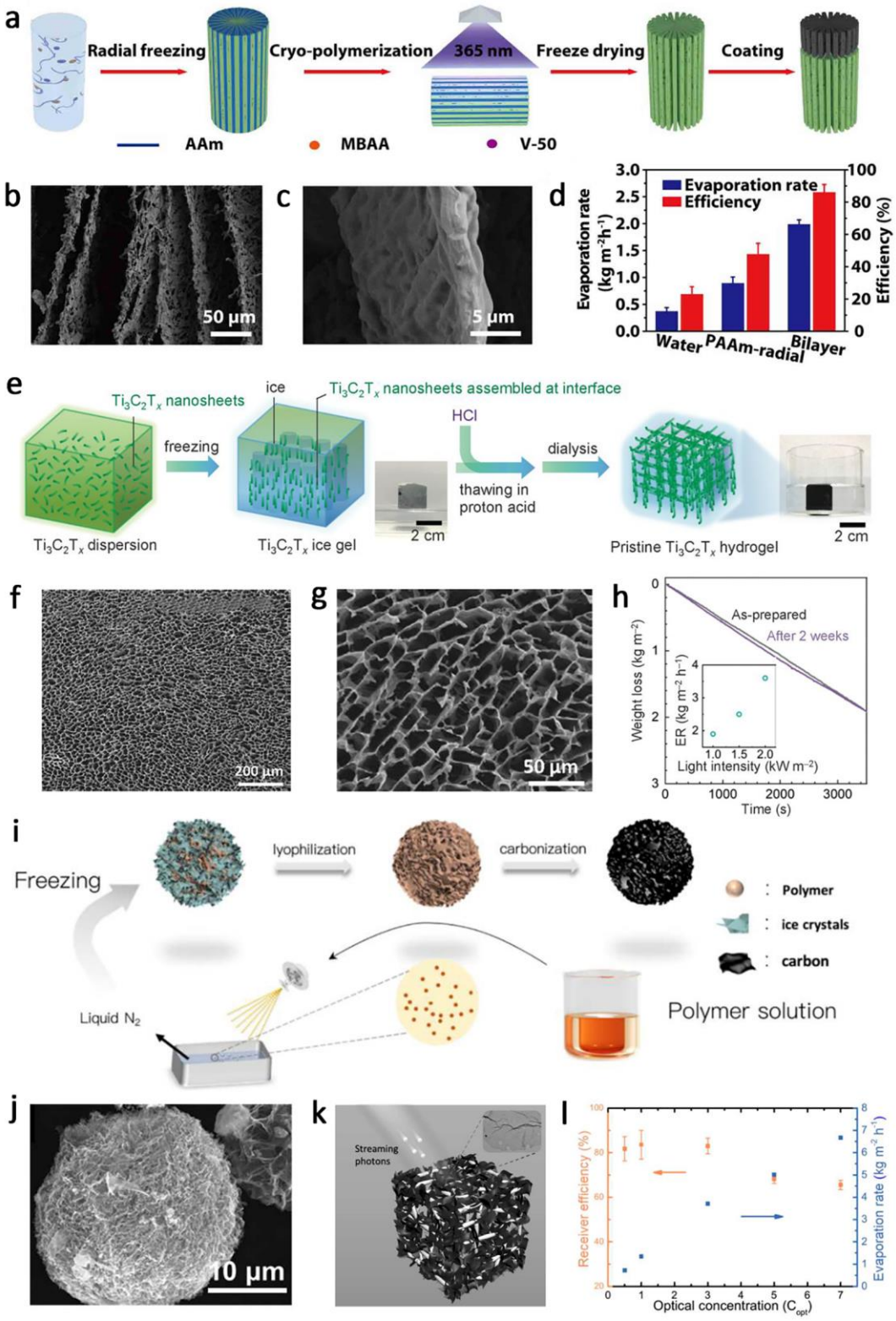

Figure 16. a) Schematic illustration of fabricating a PAAm-radial aerogel. b,c) SEM images of the PAAm-radial aerogel. d) Evaporation rates and efficiency of pure water, single PAAm-radial and bilayer aerogels. Reproduced with permission.[56] Copyright 2019, American Chemical Society. e) Schematic illustration of fabricating a pristine $Ti_3C_2T_x$ hydrogel. f,g) SEM images of the pristine $Ti_3C_2T_x$ hydrogel. h) Stability and steam generation of the $Ti_3C_2T_x$ hydrogel under different sun illumination. Reproduced with permission.[131] Copyright 2020, American Chemical Society. i) Schematic illustration of fabricating ASC material. j) SEM images of ASC material. k) Internal structure of ASC/PU. l) Receiver efficiency and evaporation rate of ASC/PU under a range of

light intensities. Reproduced with permission.[132] Copyright 2020, Elsevier.

4.4. Fuel cell

Fuel cells are is a type of power-generating devices that directly convert chemical energy in fuel into electrical energy, consisting of an oxidant electrode as anode, a fuel electrode as cathode, and a current collector separated by an electrolyte membrane.[11,105] With noble metal-based materials as electrocatalysts in the energy conversion system, they have the advantages of simple structures and effective power supply. However, the high cost and low dependability of electrode materials severely restrict their large-scale practical production and commercial application.[133] The conductivity and durability of fuel cells with non-noble metal-based materials as bifunctional electrocatalysts have been verified by oxygen evolution reaction (OER) and oxygen reduction reaction (ORR). As a consequence, composites with 3D honeycomb-like macromorphology which are fabricated with functional nanomaterials by integrative ice frozen assembly are found capable of improving the activity of bifunctional (OER and ORR) electrocatalysts.[134]

Jiang et al. conducted vacuum filtration to form a hybrid fiber membrane with $NiCoO_2$ precursor and partially rGO nanosheets. This process was subsequently developed further by integrating oil bath with ice-templating to ultimately produce 3D porous honeycomb-like $NiCoO_2$/graphene (NC-GN) network (**Figure 17**a).[105] Due to the effective facilitative effect of the bifunctional (OER and ORR) electrocatalysts in the energy conversion of the fuel cell setup as well as strong sustainability, the researchers designed and produced aligned porous fibers assembled from Co-based oxides with a low cost and long-term stability. Benefiting from the integrative ice frozen assembly, the as-obtained hierarchical lamellar structures exhibited highly favorable properties of superior pore size, high specific surface area, and strong bridging bonds (Figure 17b). The unique network structure provided NC-GN with excellent electrode activity (1.07 V) under the potential change of −3 mA cm^{-2} for ORR and the current density of 10 mA cm^{-2} for OER (Figure 17c). In addition, the electrodes of fuel cells are traditionally based on Pt catalysts, but corrosion on the surface caused by Co cannot properly exhibit their electrochemical properties. To solve these issues, Zan et al. selected gelatin as carbon/nitrogen precursor (NCNS) and red phosphorus as a dopant for the controlled synthesis of 2D carbon nanosheets (P-NCNS) as ORR electrocatalysts for fuel cells by ice/salt dual-template method (Figure 17d).[135] Notably, as shown in Figure 17e,f, the resultant uniform micro/mesoporous P-NCNS showed a quantitatively matchable pore size (0.9–5.0 nm) and a high specific surface area (499.5 m^2 g^{-1}), which delivered superior electrode activity (0.867 V) and current density (5.50 mA cm^{-2}) toward the ORR reactants in solution (Figure 17g).

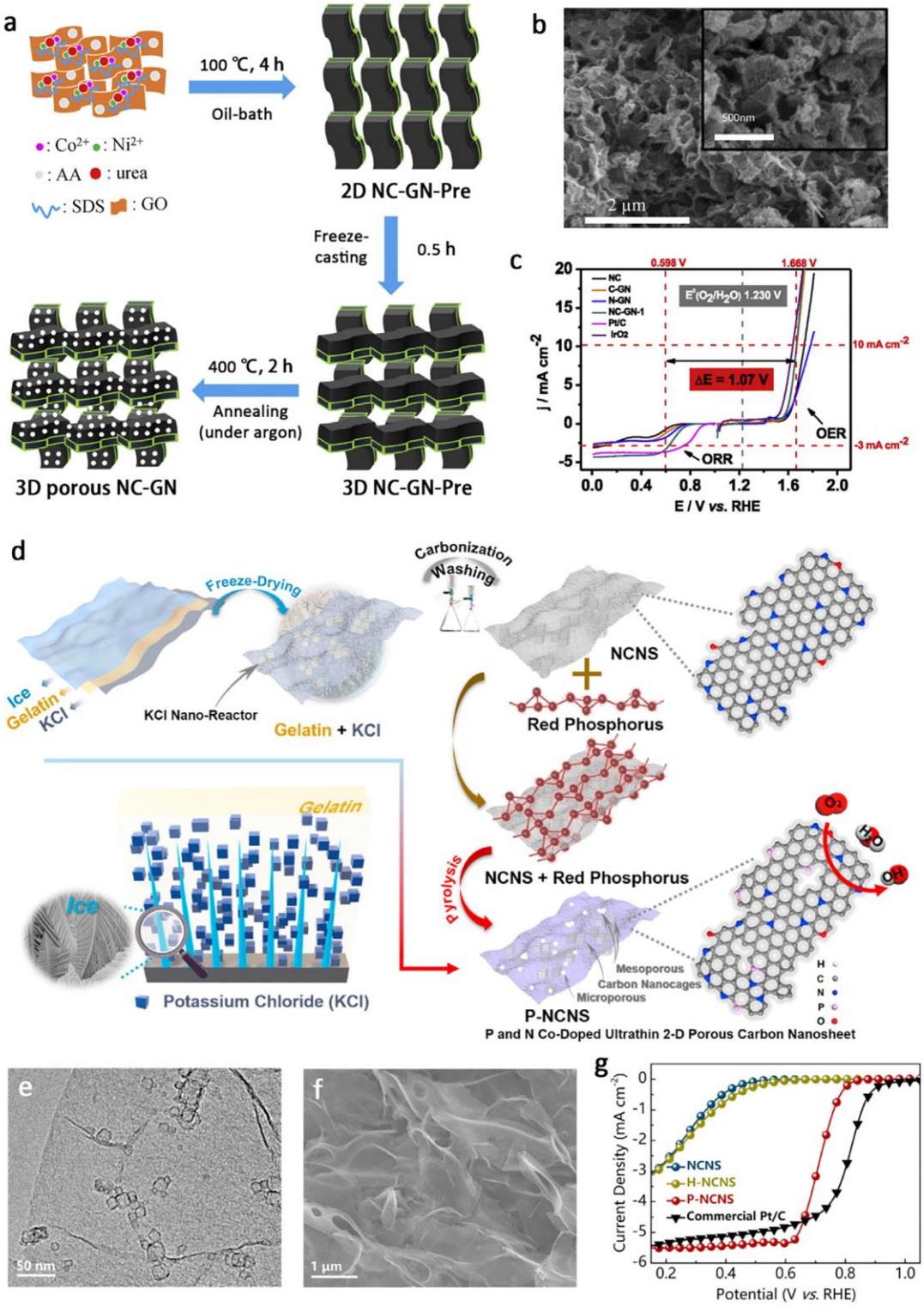

Figure 17. a) Schematic illustration of fabricating 3D porous cellular $NiCoO_2$/graphene (NC-GN) network. b) SEM image of NC-GN network. c) Comparison with different samples in terms of OER and ORR. Reproduced with permission.[105] Copyright 2018, Elsevier. d) Schematic illustration of fabricating P-NCNS electrocatalyst. e,f) SEM images of P-NCNS electrocatalyst. g) Rotating disk electrode (RDE) voltammograms of different samples. Reproduced with permission.[135] Copyright 2021, Elsevier.

5. Summary and outlook

Herein, this review well expounds on the relationship between integrative ice frozen assembly and structure and

describes the fine regulation and precise design of local pore orientation and pore morphology (honeycomb-like, lamellar, and radial) via ice-templating. The superior synergistic strengthening effect is the core of the fundamental principles underlying ice-templating integrating with other materials' processing technologies (spray, spinning, filtration, and hydrothermal) to tailor the pore geometries of scaffolds without damaging their excellent performance. Considering the performance of electrochemical storage and conversion, various porous materials with rich surface active sites, sufficient pathways for rapid electrolyte ion/electron transport, and effective stress buffering have been designed through optimizing the relationship between structures and properties.

Integrative ice frozen assembly has considerable significance for preparing state-of-art porous materials applicable in electrochemical energy storage and conversion devices. However, there are some challenges in its practical preparation and industrial applications. 1) Since facile strategies of integrative ice frozen assembly have been developed for the precise regulation of structures composed of functional nanomaterials, excellent scaffolds should be accurately prepared according to desired properties and structural characteristics. 2) In recent years, combining ice-templating with other materials' processing technologies becomes a major trend, especially with solvent-containing technologies. The fundamental principles of integrative ice frozen assembly should be further investigated to accurately capture functional composites with desired microstructure (cellular, dendritic, and lamellar) and macromorphology (0D, 1D, 2D, and 3D). 3) To precisely fabricate scaffold structures to facilitate the scale-up application by integrative ice frozen assembly, researchers should rationally design the quantitative matching of inactive components and porous materials while elucidating the synergistic mechanism of structure–orientation–property relationships in functional composites, which is expected in optimizing the electrochemical performance of porous materials to promote industrialization. In conclusion, integrative ice frozen assembly improves the economic utilization of renewable energy for electrochemical energy storage and conversion and can further enhance the practicality of functional nanomaterials for the design of multi-scale porous materials.

Acknowledgements

This research was funded by the National Natural Science Foundation of China (Grant Nos: 32001260, 12104015), the Technology Innovation Project of Jilin Province Science and Technology Department (Grant No: 2020040323SF), the Science and Technology Project of Jilin Province Education Department (Grant No: 1658131867875), and the China Scholarship Council (Grant Nos: CSC202008220178, CSC202008220179).

Conflict of Interest

The authors declare no conflict of interest.

References

[1] H. Fan, S. Zhou, Q. Wei, X. Hu, *Renew. Sust. Energ. Rev.* **2022**, 165, 112585.

[2] L. Giordano, K. Akkiraju, R. Jacobs, D. Vivona, D. Morgan, Y. S. Horn, *Accounts Chem. Res.* **2022**, 55, 298.

[3] G. Notton, M. L. Nivet, C. Voyant, C. Paoli, C. Darras, F. Motte, A. Fouilloy, *Renew. Sust. Energ. Rev.* **2018**, 87, 96.

[4] Z. Hao, Q. Zhang, X. Xu, Q. Zhao, C. Wu, J. Liu, H. Wang, *Nanoscale* **2020**, 12, 15923.

[5] D. V. Cuong, B. M. Matsagar, M. Lee, M. S. A. Hossain, Y. Yamauchi, M. Vithanage, B. Sarkar, Y. S. Ok, K. C. W. Wu, C. H. Hou, *Renew. Sust. Energ. Rev.* **2021**, 145, 111029.

[6] M. Xu, A. Wang, Y. Xiang, J. Niu, *J. Clean. Prod.* **2021**, 315, 128110.

[7] Y. Yan, G. Chen, P. She, G. Zhong, W. Yan, B. Y. Guan, Y. Yamauchi, *Adv. Mater.* **2020**, 32, 2004654.

[8] N. Zhao, M. Li, H. Gong, H. Bai, *Sci. Adv.* **2020**, 6, eabb4712.

[9] G. Shao, D. A. H. Hanaor, X. Shen, A. Gurlo, *Adv. Mater.* **2020**, 32, 1907176.

[10] H. Joukhdar, A. Seifert, T. Jüngst, J. Groll, M. S. Lord, J. R. Kovacina, *Adv. Mater.* **2021**, 33, 2100091.

[11] J. S. Yeon, N. Gupta, P. Bhattacharya, H. S. Park, *Adv. Funct. Mater.* **2022**, 32, 2112509.

[12] X. Xie, Y. Zhou, H. Bi, K. Yin, S. Wan, L. Sun, *Sci. Rep.* **2013**, 3, 2117.

[13] Y. E. Shin, Y. J. Sa, S. Park, J. Lee, K. H. Shin, S. H. Joo, H. Ko, *Nanoscale* **2014**, 6, 9734.

[14] B. B. Mandal, E. S. Gil, B. Panilaitis, D. L. Kaplan, *Macromol. Biosci.* **2013**, 13, 48.

[15] C. Ferraro, E. Garcia-Tuñon, V. G. Rocha, S. Barg, M. D. Fariñas, T. E. G. Alvarez-Arenas, G. Sernicola, F. Giuliani, E. Saiz, *Adv. Funct. Mater.* **2016**, 26, 1636.

[16] P. Divakar, K. Yin, U. G. K Wegst, *J. Mech. Behav. Biomed.* **2019**, 90, 350.

[17] X. Zho, L. Yin, B. Yang, C. Chen, W. Chen, Y. Xie, X. Yang, J. T. Pham, S. Liu, L. Xue, *Small Methods* **2021**, 5, 2000963.

[18] K. L. Scotti, D. C. Dunand, *Prog. Mater. Sci.* **2018**, 94, 243.

[19] Y. F. Tang, G. S. Grest, S. F. Cheng, *Langmuir* **2019**, 35, 4296.

[20] S. Homma, U. Yoshida, H. Nakano, *J. Phys. Soc. Jpn.* **1981**, 50, 2175.

[21] M. C. Gutiérrez, M. L. Ferrer, F. D. Monte, *Chem. Mater.* **2008**, 20, 634.

[22] P. W. Bates, X. Chen, X. Deng, *Electron. J. Differ. Eq.* **1995**, 11, 1.

[23] Z. Y. He, K. Liu, J. J. Wang, *Accounts Chem. Res.* **2018**, 51, 1082.

[24] Z. S. Zhang, X. Y. Liu, *Chem. Soc. Rev.* **2018**, 47, 7116.

[25] J. Liu, C. Q. Zhu, K. Liu, Y. Jiang, Y. L. Song, J. S. Francisco, X. C. Zeng, J. Wang, *P. Natl. Acad. Sci.* **2017**, 114, 11285.

[26] J. B. Boreyko, R. R. Hansen, K. R. Murphy, S. Nath, S. T. Retterer, C. P. Collier, *Sci. Rep.* **2016**, 6, 19131.

[27] A. Kirillova, L. Ionov, I. V. Roisman, A. Synytska, *Chem. Mater.* **2016**, 28, 6995.

[28] H. Zhang, *Ice Templating and Freeze-Drying for Porous Materials and Their Applications*, Wiley-VCH, Weinheim, Germany, **2018**.

[29] Q. L. Loh, C. Choong, *Tissue Eng. Part B-Re.* **2013**, 19, 485.

[30] C. Korber, G. Rau, M. D. Cosman, E. G. Cravalho, *J. Cryst. Growth* **1985**, 72, 649.

[31] U. G. K. Wegst, M. A. Schecter, E. Donius, P. M. Hunger, *T. R. Soc. A.* **2010**, 368, 2099.

[32] T. Waschkies, R. Oberacker, M. J. Hoffmann, *Acta Mater.* **2011**, 59, 5135.

[33] V. Naglieri, H. A. Bale, B. Gludovatz, A. P. Tomsia, R. O. Ritchie, *Acta Mater.* **2013**, 61, 6948.

[34] K. M. Pawelec, A. Husmann, S. M. Best, R. E. Cameron, *Appl. Phys. Rev*. **2014**, 1, 021301.

[35] K. Y. Yin, P. Divakar, U. G. K. Wegst, *Biomacromolecules* **2019**, 20, 3733.

[36] J. M. Smith, V. Ness, M. M. Abbott, *J. Chem. Educ.* **1950**, 27, 584.

[37] J. M.Pardo, E. Moya-Albor, G. Ortega-Ibarra, J. Brieva, *Measurement* **2020**, 151, 107085.

[38] M. Akyurt, G. Zaki, B. Habeebullah, *Energ. Convers. Manage.* **2002**, 43, 1773.

[39] D. V. Alexandrov, *J. Phys. A-Math. Theor.* **2017**, 50, 345101.

[40] G. Jia, Y. Chen, A. Sun, V. Orlien, *Rev. Food Sci. F.* **2022**, 21, 2433.

[41] P. Chitnelawong, F. Sciortino, P. H. Poole, *J. Chem. Phys*. **2019**, 150, 234502.

[42] T. Bartels-Rausch, V. Bergeron, J. H. E. Cartwright, R. Escribano, J. L. Finney, *Rev. Mod. Phys.* **2012**, 84, 885.

[43] A. K. Soper, *Science* **2002**, 297, 1288.

[44] S. Deville, *Freezing Colloids: Observations, Principles, Control, and Use: Applications in Materials Science, Life Science, Earth Science, Food Science, and Engineering*, Springer, Berlin, Germany **2017.**

[45] P. Bhattacharya, M. Kota, D. H. Suh, K. C. Roh, H. S. Park, *Adv. Energy Mater.* **2017**, 7, 1700331.

[46] J. Yang, W. Yang, W. Chen, X. Tao, *Prog. Polym. Sci.* **2020**, 109, 101289.

[47] G. Gao, S. Yang, S. Wang, L. Li, *Scripta Mater.* **2022**, 213, 114605.

[48] C. Huang, M. Dontigny, K. Zaghib, P. S. Grant, *J. Mater. Chem. A* **2019**, 7, 21421.

[49] H. Gao, L. Xu, F. Long, Z. Pan, Y. X. Du, Y. Lu, J. Ge, S. H. Yu, *Angew. Chem.* **2014**, 126, 4649.

[50] E. Munch, E. Saiz, A. P. Tomsia, S. Deville, *J. Am. Ceram. Soc.* **2009**, 92, 1534.

[51] F. Ram, B. Biswas, A. Torris, G. Kumaraswamy, K. Shanmuganathan, *Cellulose* **2021**, 28, 6323.

[52] Z. Wu, Z. R. Zhou, Y. L. Hong, *J. Adv. Ceram.* **2019**, 8, 256.

[53] X. C. Li, Z. H. Yang, Y. Peng, F. F. Zhang, M. Q. Lin, J. Zhang, Q. C. Lv, Z. X. Dong, *ACS Appl. Mater. Inter.* **2022**, 14, 11789.

[54] X. Y. Liang, G. D. Chen, S. T. Lin, J. J. Zhang, L. Wang, P. Zhang, Y. Lan, J. Liu, *Adv. Mater.* **2022**, 34, 2107106.

[55] Z. P. Xu, M. R. Wu, W. W. Gao, H. Bai, *Sci. Adv.* **2022**, 8, eabo0946.

[56] W. Z. Xu, Y. Xing, J. Liu, H.P. Wu, Y. Cuo, *ACS Nano* **2019**, 13, 7930.

[57] X. D. Wei, X. H. Cao, Y. L. Wang, G. Q. Zheng, K. Dai, C. T. Liu, C. Y. Shen, *Compos. Sci. Technol.* **2017**, 149, 166.

[58] H. X. Shang, A. Mohanram, R. K. Bordia, *J. Am. Ceram. Soc.* **2015**, 98, 3424.

[59] Y. S. Zhao, Y. Alsaid, B. W. Yao, Y. C. Zhang, B. Z. Zhang, N. Bhuskute, S. W. Wu, X. M. He, *Adv. Funct. Mater.* **2020**, 30, 1909133.

[60] M. A. Shahbazi, M. Ghalkhani, H. Maleki, *Adv. Eng. Mater.* **2020**, 22, 2000033.

[61] H. Bai, Y. Chen, B.Delattre, A. P. Tomsia, R. O. Ritchie, *Sci. Adv.* **2015**, 1, 1500849.

[62] L. Alison, S. Menasce, F. Bouville, E. Tervoort, I. Mattich, A. Ofner, A. R. Studart, *Sci. Rep.* **2019**, 9, 1.

[63] X. Y. Yang, L. H. Chen, Y. Li, J. C. Rooke, C. Sanchez, B. L. Su, *Chem. Soc. Rev.* **2017**, 46, 481.

[64] K. Y. Yin, P. Divakar, J. Hong, K. L. Moodie, J. M. Rosen, C. A. Sundback, M. K. Matthew, U. G. K. Wegst, *MRS Adv.* **2018**, 3, 1677.

[65] H. Bai, D. Wang, B. Delattre, W. W. Gao, J. D. Coninck, S. Li, A. P. Tomsia, *ACTA Biomater.* **2015**, 20, 113.

[66] K. Y. Yin, P. Divakar, U. G. K. Wegst, *ACTA Biomater.* **2019**, 84, 231.

[67] J. S. Yeon, S. Yun, J. M. Park, H. S. Park, *ACS Nano* **2019**, 13, 5163.

[68] S. Yun, S. M. Bak, S. Kim, J. S. Yeon, M. G. Kim, X. Q. Yang, P. V. Braun, H. S. Park, *Adv. Energy Mater.* **2019**, 9, 1802816.

[69] J. Zhang, L. Lin, H. Cui, *Nanomaterials* **2020**, 10, 1780.

[70] P. Nakhanivej, S. K. Park, K. H. Shin, S. Yun, H. S. Park, *J. Power Sources* **2019**, 436, 226854.

[71] M. He, G. X. Fei, Z. Zheng, Z. G. Cheng, Z. H. Wang, H. S. Xia, *Langmuir* **2019**, 35, 3694.

[72] M. Dilamian, M. Joghataei, Z. Ashrafi, C. Bohr, S. Mathur, H. Maleki, *Appl. Mater. Today* **2021**, 22, 100964.

[73] H. Y. Chi, N. Y. Chang, C. Li, V. Chan, J. H. Hsieh, Y. H. Tsai, T. Lin, *Polymers* **2022**, 14, 2610.

[74] Y. Wang, Y. Liu, Y. Liu, Q. Shen, C. Chen, F. Qiu, P. Li, L. Jiao, X. Qu, *J. Energy Chem.* **2021**, 54, 225.

[75] T. Pirzada, Z. Ashrafi, W. Y. Xie, S. A. Khan, *Adv. Funct. Mater.* **2020**, 30, 1907359.

[76] N. Awang, J. Jaafar, A. F. Ismail, *Polymers* **2018**, 10, 194.

[77] F. Zoller, S. Häringer, D. Böhm, H. Illner, M. Döblinger, Z. Sofer, M. Finsterbusch, T. Bein, D. Fattakhova-Rohlfing, *Adv. Funct. Mater.* **2021**, 31, 2106373.

[78] T. Xu, Y. C. Ding, Z. P. Liang, H. L. Sun, F. Zheng, Z. T. Zhu, Y. Zhao, H. Fong, *Prog. Mater. Sci.* **2020**, 112, 100656.

[79] L. Wang, H. Lv, L. Liu, Q. Zhang, P. Nakielski, Y. Si, J. Cao, X. Li, F. Pierini, J. Yu, B. Ding, *J. Colloid Interf. Sci.* **2020**, 565, 416.

[80] C. X. Li, J. Yang, P. Pachfule, S. Li, M. Y. Ye, J. Schmidt, A. Thomas, *Nat. Commun.* **2020**, 11, 1.

[81] Y. Cui, H. X. Gong, Y. J. Wang, D. W. Li, H. Bai, *Adv. Mater.* **2018**, 30, 1706807.

[82] Z. Xu, Y. Zhang, P. G. Li, C. Gao, *ACS Nano* **2012**, 6, 7103.

[83] F. A. Formica, E. Özturk, S. C. Hess, W. J. Stark, K. Maniura-Weber, Rottmar, M. M. Zenobi-Wong, *Adv. Healthc. Mater.* **2016**, 5, 3129.

[84] L. Lin, J. Cao, J. Zhang, Q. Cui, Y. Liu, *Nanomaterials* **2020**, 10, 682.

[85] W. Guo, C. Cheng, Y. Z. Wu, Y. A. Jiang, J. Gao, D. Li, L. Jiang, *Adv. Mater.* **2013**, 25, 6064.

[86] W. W. Gao, M. N. Wang, H. Bai, *J. Mech. Behav. Biomed.* **2020**, 109, 103820.

[87] J. Zhang, H. Zhu, X. Wu, H. Cui, D. Li, J. Jiang, C. Gao, Q. Wang, Q. Cui, *Nanoscale* **2015**, 7, 10807.

[88] J. M. Jeong, H. G. Kang, H. J. Kim, S. B. Hong, H. Jeon, S. Y. Hwang, D. Seo, B. E. Kwak, Y. K. Han, B. G. Choi, D. H. Kim, *Adv. Funct. Mater.* **2018**, 28, 1802952.

[89] J. Li, Q. Shi, J. A Röhr, H. Wu, B. Wu, Y. Guo, Q. Zhang, C. Hou, Y. Li, H. Wang, *Adv. Funct. Mater.* **2020**, 30, 2002508.

[90] Y. Shao, M. F. El-Kady, C. Lin, G. Zhu, K. L. Marsh, J. Y. Hwang, Q. Zhang, Y. Li, H. Wang, R. B. Kaner, *Adv. Mater.* **2016**, 28, 6719.

[91] Y. Xu, C. Huang, A. Hu, Z. Fan, C. Chen, Y. Yang, Q. Tang, C. Jiang, X. Chen, *Appl. Surf. Sci.* **2021**, 563, 150303.

[92] F. Xue, X. D. Qi, T. Huang, C. Y. Tang, N. Zhang, Y. Wang, *Chem. Eng. J.* **2021**, 419, 129620.

[93] A. Chakraborty, A. T. Mulroney, M. C. Gupta, *Rev. Adhes. Adhes.* **2021**, 9, 35.

[94] G. W. Zhang, Z. M. Liu, X. Yuan, Y. Q. He, N. Wei, H. F. Wang, B. Zhang, *J. Hazard. Mater.* **2022**, 430, 128374.

[95] S. Zhao, H. B. Zhang, J. Q. Luo, Q. W. Wang, B. Xu, S. Hong, Z. Z. Yu, *ACS Nano* **2018**, 12, 11193.

[96] Y. Lin, Q. Kang, H. Wei, H. Bao, P. K. Jiang, Y. W. Mai, X.Y. Huang, *Nano-Micro Lett.* **2021**, 13, 1.

[97] O. A. Ibrahim, M. Navarro-Segarra, P. Sadeghi, N. Sabate, J. P. Esquivel, E. Kjeang, *Chem. Rev.* **2022**, 122, 7236.

[98] N. R. Hemanth, R. D. Mohili, M. Patel, A. H. Jadhav, K. Lee, N. K. Chaudhari, *J. Mater. Chem. A* **2022**, 10, 14221.

[99] J. F. Ni, A. Dai, Y. F. Yuan, L. Li, J. Lu, *Matter* **2020**, 2, 1366.

[100] S. Wang, Z. Yuan, Zhang X, S. S. Bi, Z. Zhou, J. L. Tian, Q. C. Zhang, Z. Q. Niu, *Angew. Chem. Int. Edit.* **2021**, 133, 7132.

[101] E. Santos, W. Schmickler, *Chem. Rev.* **2022**, 122, 10581.

[102] P. Nakhanivej, S. K. Park, K. H. Shin, S. Yun, H. S. Park, *J. Power Sources* **2019**, 436, 226854.

[103] J. Li, D. Chen, Q. Wu, X. Wang, Y. Zhang, Q. Zhang, *New J. Chem.* **2018**, 42, 4513.

[104] Q. Liu, S. Jing, S. Wang, H. Zhuo, L. Zhong, X. Peng, R. Sun, *J. Mater. Chem. A* **2016**, 4, 13352.

[105] S. Jiang, K. Ithisuphalap, X. R. Zeng, G. Wu, H. P. Yang, *J. Power Sources* **2018**, 399, 66.

[106] J. Sun, J. Huang, L. E, C. Ma, Z. Wu, Z. Xu, S. Luo, W. Li, S. Liu, *ACS Sustain. Chem. Eng.* **2020**, 8, 11114.

[107] C. Shi, L. Hu, K. Guo, H Li, T. Zhai, *Adv. Sustain. Syst.* **2017**, 1, 1600011.

[108] L. X. Li, C. Jia, X. D. Zhu, S. C. Zhang, *J. Clean. Prod.* **2020**, 256, 120326.

[109] W. Raza, F. Ali, N. Raza, Y. Luo, K. H. Kim, J. Yang, S. Kumar, A. Mehmood, E. E. Kwon, *Nano Energy* **2018**, 52, 441.

[110] S. Zhu, L. N. Wang, C. Y. Gu, H. C. Liu, Y. W. Mu, J. F. Ni, G. Y. Han, *J. Power Sources* **2022**, 532, 231335.

[111] Z. F. Lin, P. L. Taberna, P. Simon, *Curr. Opin. Electroche.* **2017**, 6, 115.

[112] T. Y. Liu, Y. Li, *InfoMat* **2020**, 2, 807.

[113] R. Naraprawatphong, C. Chokradjaroen, S. Thiangtham, L. Yang, N. Saito, *Mater. Today Adv.* **2022**, 16, 100290.

[114] B. W. Deng, Y. Yang, Y. X. Liu, B. Yin, M. B. Yang, *J. Colloid Interf. Sci.* **2022**, 618, 399.

[115] Y. F. Zheng, K. M. Chen, K. P. Jiang, F. R. Zhang, G. S. Zhu, H. R. Xu, *J. Energy Storage* **2022**, 56, 105995.

[116] C. Li, K. B. Wang, J. Z. Li, Q. C. Zhang, *Nanoscale* **2020**, 12, 7870.

[117] B. Liang, L. Chen, J. Lv, Y. Li, W. Tan, W. Zhu, J. Hu, K. Zeng, G. Yang, *ACS Appl. Energy Mater.* **2022**, 5, 6163.

[118] P. Bhattacharya, T. Joo, M. Kota, H. S. Park, *Ceram. Int.* **2018**, 44, 980.

[119] J. Xiang, Y. Wei, Y. Zhong, Y. Yang, H. Cheng, L. Yuan, H. Xu, Y. Huang, *Adv. Mater.* **2022**, 1, 2200912.

[120] Y. Han, Y. Lei, J. Ni, Y. Zhang, Z. Geng, P. Ming, C. Zhang, X. Tian, J. L. Shi, Y. G. Guo, Q. Xiao, *Small* **2022**, 1, 2107048.

[121] J. L. Cheng, G. F. Gu, Q. Guan, J. M. Razal, Z. Y. Wang, X. L. Li, B. Wang, *J. Mater. Chem. A* **2016**, 4, 2729.

[122] S. S. Zhang, *Energy Environ. Mater.* **2021**, 2, 12330.

[123] X. Yu, S. Yun, J. S. Yeon, P. Bhattacharya, L. B. Wang, S. W. Lee, X. L. Hu, H. S. Park, *Adv. Energy Mater.* **2018**, 8, 1702930.

[124] C. Li, C. Zhang, K. B. Wang, F. Yu, J. Xie, Q. C. Zhang, *Chem. Eng. J.* **2022**, 431, 133234.

[125] Y. Li, C. Wu, Y. Bai, L. Liu, H. Wang, F. Wu, N. Zhang, Y. Zou, *ACS Appl. Mater. Inter.* **2016**, 8, 18832.

[126] X. Li, S. Ling, L. Zeng, H. He, X. Liu, C. Zhang, *Adv. Energy Mater.* **2022**, 12, 2200233.

[127] Z. Xu, Z. Li, Y. Jiang, G. Xu, M. Zhu, W. C. Law, K. T. Yong, Y. Wang, C. Yang, B. Dong, F. Xing, *J. Mater. Chem. A* **2020**, 8, 25571.

[128] V. D. Dao, N. H. Vu, S. N. Yun, *Nano Energy* **2020**, 68, 104324.

[129] Y. Lu, H. Zhang, D. Q. Fan, Z. P. Chen, X. F. Yang, *J. Hazard. Mater.* **2022**, 423, 127128.

[130] G. H. Liu, T. Chen, J. L. Xu, G. Li, K. Y. Wang, *J. Mater. Chem. A* **2020**, 8, 513.

[131] H. Chen, H. Ma, P. Zhang, Y. Wen, L. Qu, C. Li, *ACS Nano* **2020**, 14, 8, 10471.

[132] D. Li, A. Li, Y. Chen, G. Chen, X. Chen, D. Zhang, H. Zhu, I. A. Samo, H. Song, *Carbon* **2020**, 162, 481.

[133] F. Jaouen, *Nat. Mater.* **2022**, 21, 733.

[134] J. M. Ju, C. H. Lee, J. H. Park, J. H. Lee, H. Lee, J. H. Shin, S. Y. Kwak, S. U. Lee, J. H. Kim, *ACS Appl. Mater. Inter.* 2**022**, 14, 24404.

[135] Y. Zan, Z. Zhang, B. Zhu, M. Dou, F. Wang, *Carbon* **2021**, 174, 404.